Project No: 603502

DACCIWA

"Dynamics-aerosol-chemistry-cloud interactions in West Africa"

Deliverable

D4.5 Model performance

<u>**Due date of deliverable:**</u>	31/05/2018
<u>**Completion date of deliverable:**</u>	04/06/2018

Start date of DACCIWA project:	1st December 2013	**Project duration:**	60 months

Version:	[V1.0]
File name:	[D4.5_Model_performance_DACCIWA_v1.0.pdf]

Work Package Number:	**4**
Task Number:	**5**

<u>**Responsible partner for deliverable:**</u>	**UNIVLEEDS**
Contributing partners:	**KIT, MO, ETHZ, ECMWF, UPMC, UNIVMAN**

Project coordinator name:	Prof. Dr. Peter Knippertz
Project coordinator organisation name:	Karlsruher Institut für Technologie

Dissemination level		
PU	Public	**x**
PP	Restricted to other programme participants (including the Commission Services)	
RE	Restricted to a group specified by the consortium (including the Commission Services)	
CO	Confidential, only for members of the consortium (including the Commission Services)	

Nature of Deliverable		
R	Report	**x**
P	Prototype	
D	Demonstrator	
O	Other	

Copyright

DOCUMENT INFO

Authors

Author	Beneficiary Short Name	E-Mail
John Marsham, Phil Rosenberg	UNIVLEEDS	J.Marsham@leeds.ac.uk
Paul Field	MO	paul.field@metoffice.gov.uk
Bernhard Vogel	KIT	bernhard.vogel@kit.edu
Angela Benedetti	ECMWF	Angela.Benedetti@ecmwf.int
Laurent Menut, Cyrille Flamant, Adrian Deroubaix	UPMC	menut@lmd.polytechnique.fr
Hugh Coe	UNIVMAN	Hugh Coe <hugh.coe@manchester.ac.uk
Tanya	ETHZ	tanjast <tanja.stanelle@env.ethz.ch

Changes with respect to the DoW

Issue	Comments
-	-

Dissemination and uptake

Target group addressed	Project internal / external
Scientific	Internal and external

Document Control

Document version #	Date	Changes Made/Comments
V0.1	26.03.18	Template with basic structure
V0.2	18.05.18	Final version including all contributions to be approved by the general assembly
V0.3	04.06.18	Version approved by the general assembly

Table of Content

1   Introduction

Southern West Africa presents a unqiue environment for clouds, aerosols and cloud-aerosol interactions. A shortgage of data has meant that details of models have been largely untested in this region. DACCIWA has delivered an unrivalled dataset formodel evaluation. This reports summarises main results from DACCIWA deliverable D4.5 to date, showing how varied models perform at describing the regional aerosol and cloud systems across the region and an examination of the model performance at capturing the interactions between aerosols clouds and precipitation.

2   Models and Observations used

This section outlines the modelling systems used, together with observations used to evaluate them. Where systems have already been described in the D4.4 report the reader is referred to that report for details.

2.1   The aerosol climate model ECHAM6-HAM2 (ETHZ)

The ECHAM6-HAM2 model is a global aerosol climate model. ECHAM6 is the sixth generation of the atmospheric general circulation model ECHAM. It is described in detail in Stevens et al. (2013). ECHAM6 employs a spectral transform dynamical core and a flux-form semi-Lagrangian tracer transport algorithm from Lin and Rood (1996). Vertical mixing occurs through turbulent mixing, moist convection (including shallow, deep, and mid-level convection), and momentum transport by gravity waves arising from boundary effects or atmospheric disturbances. Sub-grid scale cloudiness (stratiform clouds) is represented using the scheme of Sundqvist (1989) which calculates diagnostically the grid cell cloud fraction as a function of the relative humidity in the given grid cell, once a threshold value is exceeded. Liquid (cloud water) and solid (ice water) condensates are treated prognostically following Lohmann and Roeckner (1996). Radiative transfer in ECHAM6 is represented using the radiation transfer broadband model (RRTMG), which considers 16 and 14 bands for the shortwave (820 to 50000 cm-1) and longwave (10 to 3000 cm-1) parts of the spectrum, respectively (Iacono et al., 2008).

The aerosol module HAM was first implemented in the 5th generation of ECHAM (ECHAM5; Roeckner et al., 2003) by the Max Planck Institute for Meteorology (Stier et al, 2005). Over the past years, the HAM module has been improved and completed with new processes (HAM2) as described in Zhang et al. (2012). The HAM2 module is now coupled to the ECHAM6.

Aerosol microphysics is simulated using the M7 module (Vignati et al., 2004), which accounts for sulfate, black carbon, particulate organic matter, sea salt, and dust. The atmospheric aerosol population is described as a superposition of seven lognormal distributed modes for which standard deviations are prescribed. The total number concentration and masses of the different chemical components are prognostic variables in the model. The modes are divided into soluble, internally mixed modes (containing sulfate) and insoluble, externally mixed modes, which are assigned to different size ranges. The modal diameters can vary and are calculated at each time step from the mass and number concentrations for each mode. Dust particles are considered as part of the soluble and insoluble accumulation and coarse modes. Sedimentation and dry and wet deposition are parameterized as functions of the aerosol size distribution, composition, and mixing state and depend on the ECHAM6 meteorology. The emission fluxes of dust, seasalt, and dimethyl sulfide from the oceans (DMS) are calculated online, based on the model meteorology. Anthropogenic emissions are prescribed.

The optical properties of the modelled aerosol concentrations are employed in the radiative transfer calculations. The aerosol activation and ice nucleation parameterizations of the two-moment stratiform cloud scheme of Lohmann et al. (2007) provide links between the simulated aerosol population and the number concentrations of cloud droplet and ice crystal. The model accounts for aerosol effects on cloud microphysics (droplet number and size) and macrophysics (liquid water path).

For the DACCIWA project we choose to perform model simulations with the recent developed model version ECHAM6.3-HAM2.3. We performed simulations in T63L47 resolution (approx. 200 km x 200 km horizontal resolution). In deliverable 4.3 a nudged simulation (nudged with ERAinterim reanalysis) were already evaluated. In this deliverable, we present simulations performed in free mode, which means that the large-scale circulation is not prescribed. The model is able to account for feedbacks between aerosols and the atmosphere (via the direct and indirect aerosol effect). But the sea surface temperature (SST) and the sea ice cover (SIC) are prescribed by AMIP data (https://pcmdi.llnl.gov/mips/amip/amip2/). Therefore, the SST and SIC are not able to adjust to changes in the atmosphere. The performed simulations differ in the applied emission inventory, they are summarized in table 2.1.1. Emission fluxes of the year 2010 are read in for the entire simulation period.

Table 2.1.1: Performed simulations. GFAS biomass burning emission fluxes are multiplied by a factor of 3.4 as recommended by Kaiser et al (2012).

	Anthropogenic emissions	Biomass burning emissions
accmip	ACCMIP (Lamarque et al., 2010)	ACCMIP (Lamarque et al., 2010)
accmip_gfas	ACCMIP (Lamarque et al., 2010)	GFAS (Heil et al., 2010)
htap	HTAP (http://edgar.jrc.ec.europa.eu/htap_v2/)	GFAS (Heil et al., 2010)
ceds	CEDS (http://www.globalchange.umd.edu/ceds/)	GFAS (Heil et al., 2010)
dacciwa	DACCIWA (WP2, deliverable 2.1)	GFAS (Heil et al., 2010)

2.2 ECMWF's Coupled Ensemble Prediction System

Sub-seasonal forecasts out to 46 days have been produced routinely at ECMWF since March 2002, and operationally since October 2004 (Vitart, 2014). In the current configuration, the monthly forecasts are generated by extending the 15-day ensemble integrations to 46 days twice a week (at 00UTC on Mondays and Thursdays). Forecasts are based on the medium range/monthly ensemble forecast (ENS) which is part of ECMWF's Integrated Forecasting System. ENS includes 51 members run with a horizontal resolution of TCo639 (about 16 km) up to forecast day 15, and TCo319 (about 32 km) thereafter. The atmospheric model is coupled to an ocean model (NEMO) with a 1/4 degree horizontal resolution.

After a few days of model integrations, the model mean climate begins to be different from the initial conditions. No bias-correction is applied to remove or reduce the drift in the model, and no steps are taken to remove or reduce any imbalances in the coupled model initial state. The effect of the drift

on the model calculations is estimated a posteriori from integrations of the model in previous years (re-forecasts) and removed (calibration). The climatology which is provided by the re-forecasts is computed using a suite that includes only 11 members of 46-day integrations with the same configuration as the real-time forecasts, starting on the same day and month as the real-time forecast over the past 20 years. For the model integrations presented in this study, the re-forecasts are run with 10 ensemble members over a shorter period (2003-2015) due to the limited availability of the aerosol emissions.

Initial perturbations are generated using a combination of singular vectors and perturbations generated using the ECMWF ensemble of data assimilations, and model uncertainties are simulated using two stochastic schemes (Leutbecher et al. 2017). The aerosol fields are not perturbed in the different ensemble members. However for natural aerosols such as desert dust and sea-salt, whose emissions are parameterized based on meteorological variables, most prominently winds, any perturbations on those will also reflect on perturbations on the aerosol emissions themselves.

The ECMWF/CAMS aerosol model

In the context of the Copernicus Atmosphere Monitoring Service, and precursors projects GEMS and MACC, ECMWF has developed a capability to monitor and forecast atmospheric composition, including aerosols, greenhouse gases and reactive gases, using satellite observations and a combination of global and regional models. The atmospheric composition prediction system is based on the Integrated Forecast System (IFS) meteorological model, maintained and developed by ECMWF. The version used in this work corresponds to cycle 43R1 of the IFS for which a detailed description can be found on the ECMWF's webpage (https://software.ecmwf.int/wiki/display/FCST/Implementation+of+IFS+Cycle+43r1). Generally IFS is not run with the full coupled chemistry due to its computational cost. Currently the operational resolution of IFS with full chemistry is 40 km with 60 vertical level up to 0.1 hPa as opposed to the operational NWP without full chemistry which has a resolution of 9km and 137 vertical levels up to 0.01 hPa. Aerosols are forecast within the global system by a bulk/bin scheme (Morcrette *et al* 2008), based on earlier work by Reddy *et al* (2005) and Boucher et al (2002), that includes five species: dust, sea salt, black carbon, organic carbon and sulfates. Dust aerosols are represented by three prognostic variables that correspond to three size bins, with bin limits of 0.03, 0.55, 0.9 and 20 microns in radius. Sea-salt aerosols are also represented by three size bins with limits of at 0.03, 0.5, 5 and 20 microns in radius. Emissions of natural aerosols such as desert dust and sea salt are parameterized based on model variables with surface winds being the main driver.

For all other tropospheric aerosols (carbonaceous aerosols and sulfates), emission sources are defined according to established inventories (Lamarque et al 2010). Biomass burning emissions contributing to black carbon and organic matter loads are prescribed from the Global Fire Assimilation System (GFAS, Kaiser et al 2012}). Removal processes include sedimentation of all particles, wet and dry deposition and in-cloud and below cloud scavenging.

For organic matter and black carbon, both the hydrophobic and hydrophilic components are considered. A very simplified representation of the sulfur cycle is also included with only two variables, sulfur dioxide (SO_2) and sulphate (SO_4), this latter one in the particulate phase. Overall, a total of 12 additional prognostic variables for the mass mixing ratio of the different components (bins or types) of the various aerosols are used in this configuration. Several revisions of the dust emission schemes have been undertaken as well as developments to include more aerosol species, such as nitrates and secondary organic aerosols (Rémy, private communication).

In the version of the global IFS system used for DACCIWA, which was operational until July 2017, the direct radiative effect of aerosols is taken into account using the aerosol monthly climatology of Tegen et al (1997). A second control experiment was performed using the new CAMS climatology by Bozzo et al (2017) which has become operational after July 2017. In the experimental version of the system, however, the aerosol optical depth which is used to calculate the radiative impacts can be computed directly from the mass mixing ratios of the prognostic aerosols provided by the aerosol module. We make use of this capability to set-up experiments with the coupled Ensemble Prediction System as described in the next section, to investigate the importance of the direct radiative impact of the prognostic aerosols relative to control runs that uses the Tegen and the CAMS/Bozzo climatologies. We also investigate the sensitivity to initial conditions for the aerosols by choosing different datasets to initialize the simulations. Please note that the indirect aerosols effect were not investigated in these experiments as the capability is not currently supported in the ECMWF/CAMS system.

Four experiments were run to assess the aerosol impacts: one control integration with the Tegen climatology in which all settings are similar to the operational set-up, but run at lower horizontal resolution (T255 corresponding to 80km), indicated henceforth as CONTROL1; a second control run with the CAMS/Bozzo climatology at the same reduced resolution (CONTROL2); an interactive prognostic aerosol run in which the prognostic aerosols are initialized using the time-varying CAMSira, indicated as PROG1; a second interactive aerosols run in which the prognostic aerosols are initialized using a fixed climatology which is based on a CAMS experiments without any data assimilation (Flemming, private communication), indicated as PROG2. The different choice of initialization allows to understand the sensitivity of the interactive aerosol runs to the initial conditions. Neither the Tegen or the CAMS/Bozzo climatology are used in the interactive aerosol runs in which aerosols are instead allowed to interact with the radiation. Only the direct aerosol effect is taken in consideration while indirect aerosol effects on clouds are not modeled. All simulations were conducted with 91 vertical levels. Prescribed emissions for the anthropogenic species over the years of interest (2003 to 2015) were used. Updating the emissions over the course of the re-forecasts is clearly essential, particularly for biomass burning emissions which cannot be accounted for with persistence over the course of several weeks, having a natural life cycle of a few days. It is possible to take into account these emissions using climatologies. However, in this work, we have used emissions estimated from the Fire Radiative Power (FRP) provided by the MODIS instruments on board of the Aqua and Terra satellites and processed according to Kaiser et al. (2012) to obtain emission coefficients for biomass burning aerosols. As far as biomass burning emissions are concerned, these simulations represent a "best-case scenario" because emissions are based on actual observations of MODIS FRP. It would be possible to prescribe climatologies for the biomass burning to see specifically the impact of the way the biomass burning source is prescribed. Ultimately, and ideally, if one had a prognostic model for biomass burning emissions related to weather parameters, the full impact of prescribing those important emissions versus modeling them could be assessed. Currently sensitivity experiments without any biomass burning emissions are being run with an identical set-up to assess the total impact of this aerosol component.

For computational cost the size of the ensemble was limited to 10 members plus one unperturbed forecast. To ensure more robust statistics five initialization dates were considered for each year for the summer integrations (April 20, April 25, May 1, May 5, May 10). The total number of ensemble members was hence increased to 55. All runs were set-up to be six months long, although only statistics for week 1 to week 4 are presented here. The seasonal aspects will be investigated in an additional peer-reviewed paper at a later date. The meteorological variables were initialized using ERA-Interim (Dee et al. 2011), whereas the initial conditions for soil variables were taken from experiments run in-house (Balsamo, private communication).

2.3 WRF-CHIMERE (UPMC)

See D4.4 Report

2.4 Met Office Unified Model (Leeds and Met Office)

See D4.4 Report

2.5 COSMO-ART (KIT)

See D4.4 report

3 Analysis of regional aerosol and cloud systems and model performance

3.1 ECHAM analysis (ETHZ)

The regional aerosol distribution

The simulations differ between each other in terms of the applied emission inventory. As seen in figure 3.1.1, the emission inventories show substantial differences. The annual cycle is given by the biomass burning emissions, the anthropogenic fluxes do not show monthly variations. This explains the low emission fluxes in simulation "accmip" during winter. This is the only simulation where we did not apply the gfas biomass burning emission inventory (table 2.1.1). In general, the main difference between the accmip and gfas biomass burning emissions are caused by the application of the recommended factor of 3.4 by Kaiser et al. (2012). At the Guinea Coast the biomass burning emission occur during winter. But during summer a large contribution of biomass burning aerosols is transported to the Guinea Coast from their source region in central Africa.

During winter time the regional aerosol content is dominated by mineral dust particles which are emitted in the Sahara and transported into southwest Africa. There are variations in dust concentrations between the simulations. Dust emissions are calculated online in dependency of the vegetation cover, wind speed, and soil properties. The changes in the emission fluxes are caused by induced changes in wind speed due to feedbacks between aerosols, radiation, and clouds. In DACCIWA, we focus on summertime. In the boundary layer, anthropogenic plus biomass burning aerosol concentrations are in the same order of magnitude as the dust concentrations during summer (figure 3.1.2). In June – July – August – September the simulations with the highest aerosol burden in the boundary layer is "dacciwa". The lowest surface aerosol concentration is simulated in "accmip-gfas". This is staggering because the biomass burning emissions prescribed in simulation "accmip-gfas" are three times larger than the ones in "accmip". But due to feedback mechanisms the dust concentration is higher in "accmip". This points out the important need to understand the dust emission – transport – deposition processes to simulate the aerosol distribution in southwest Africa correctly.
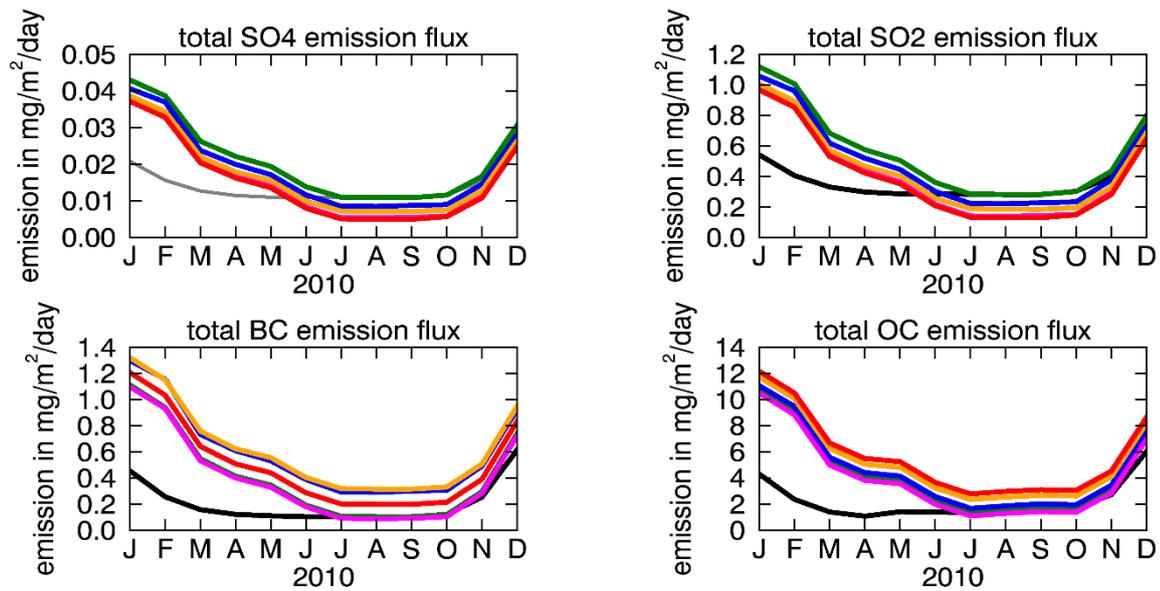
Figure 3.1.1: Mean anthropogenic aerosol emission fluxes (black: accmip; green: accmip + gfas; orange: ceds; blue: htap, red: dacciwa). The emission fluxes are averaged over a domain of 5° N – 15° N, 15° W – 15° E.

Interactions between aerosols and clouds

Nocturnal low-level clouds are a prominent feature at the Guinea Coast during the West African monsoon season. They form shortly after sunset, spread during the night and dissipate in the late morning or early afternoon. The model does not resolve them adequately, the amount of low level clouds is underestimated and their diurnal cycle is not captured by the model (figure 3.1.3). The mechanisms controlling the formation and maintenance of the low-level clouds were investigated by e.g. Schrage and Fink (2012), Schuster et al. (2013), and Adler et al. (2016). They are dominated by dynamical processes; the low-level jet, which forms during night, and the monsoon flow bring cold air with enhanced relative humidity to the coast. On a smaller scale (few hundreds to a few tenth of kilometres) clouds are triggered by orographic induced lifting, gravity waves, and horizontal convergence upstream of existing clouds. Additionally, turbulent sub-grid-scale mixing is important for the upward shift of the clouds (Adler et al., 2016). These processes are not well captured by our as well as other climate models. One reason therefore is the rather coarse resolution in most global climate models. Since aerosols, which act as cloud condensation nuclei, are usually present in our region of interest, the number of aerosols play an small part in the formation of the clouds. But small differences between the simulations are visible, which are caused by the available number of cloud condensation nuclei (figure 3.1.2 and 3.1.3).
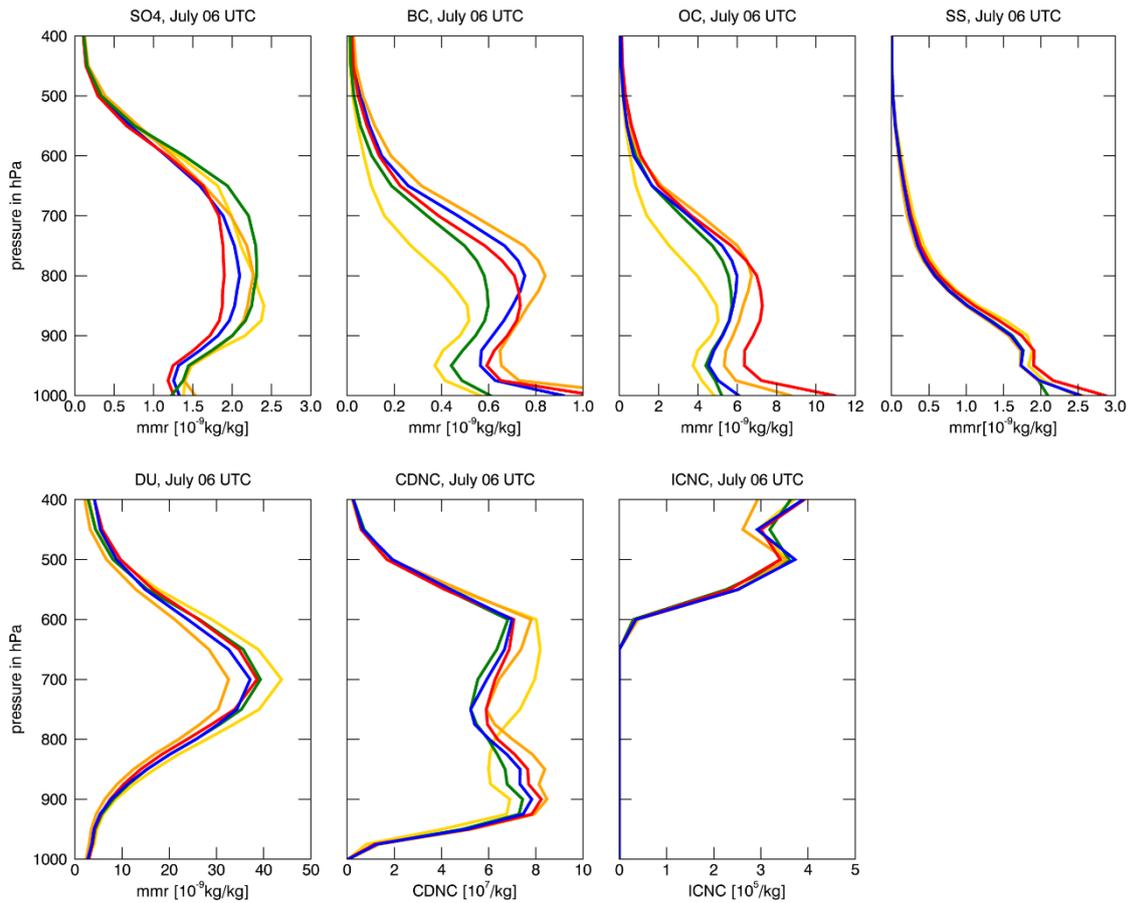
Figure 3.1.2: Simulated 10 year mean tracer concentration averaged over 8° W – 8° E, 5° N – 10° N for July, 06 UTC (gold – accmip, green – accmip_gfas, blue – htap, orange – ceds, red – dacciwa).
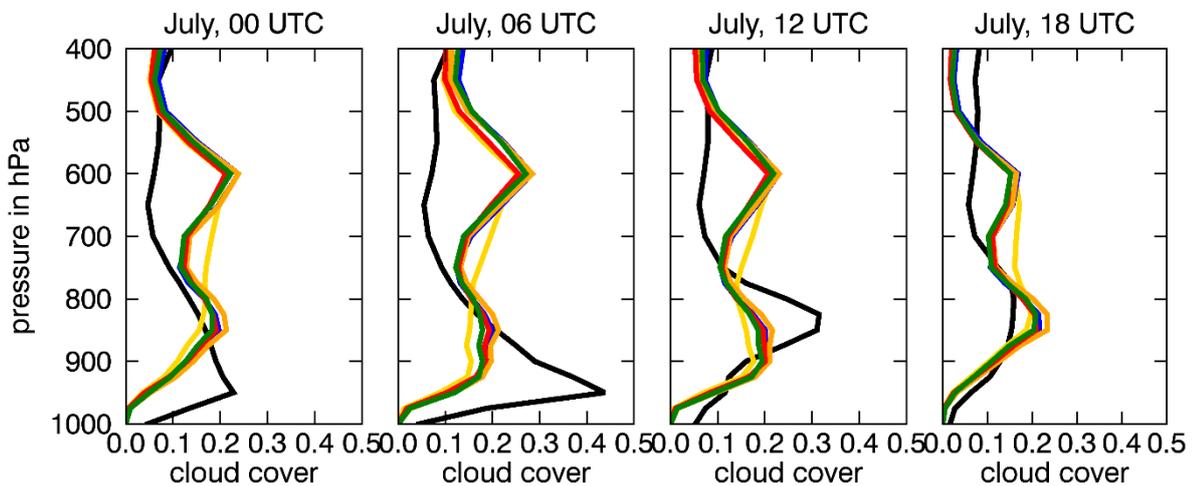
Figure 3.1.3: Simulated cloud cover averaged over 8° W – 8° E, 5° N – 10° N for July (avg. 1996-2010). The black line corresponds to ERAinterim reanalysis, coloured lines show results of the different ECHAM6-HAM2 simulations (gold – accmip, green – accmip_gfas, blue – htap, orange – ceds, red – dacciwa).

3.2 ECMWF(CAMS) model analysis (ECMWF)

Several diagnostics are applied to assess the relative skill of the experiments. These diagnostics have been developed over a number of years and are now used routinely at ECMWF to assess improvements in the EPS due to changes in various elements, for example physical parameterizations or changes in the ocean model as well as increases in vertical and horizontal

resolution. Bias plots for several meteorological parameters averaged for the weekly period starting from day 26 to day 32 (week 4) are shown in figures 3.2.1 to 3.2.3. For a start date of May 1, this corresponds to the end of May/beginning of June. The bias is estimated by computing the difference between the model weekly climatology as a function of lead time and the weekly mean climatology from ERA Interim computed over the same years (2003-2015). Biases are only shown with respect to CONTROL1.

Aerosols will directly affect lower-troposphere temperature in cloud-free regions due the radiative cooling in the shortwave. Changes in the diabatic heating profile can also occur as a result of differential warming/cooling induced by absorbing aerosols. Winds are also indirectly affected by aerosols because of the changes in the amplitude and distribution of the diabatic heating (Ramanathan et al. 2005; Lau and Kim 2010).

The bias in temperature at 850hPa for CONTROL1 is shown in figure 3.2.1 four weeks into the simulation. The change in bias for experiments PROG1 and PROG2 with respect to CONTROL1 is also shown in the same figure. Blue shades in the lower panels indicate a reduction in bias when red shades are present in corresponding regions in the top panel. Areas particularly affected are the Mediterranean basin, Central Africa, the Asian dust belt in the Northern Pacific Ocean and to a lesser extent, the North Atlantic dust belt. The Arctic also appears quite noticeably with a reduction in bias, however few grid points are actually included in that region. In some areas the temperature bias is reduced between -0.5 up to 2.0 degrees: this is particularly noticeable in the North Pacific. The bias in the Mediterranean Sea is also reduced. Generally the Northern Hemisphere appears to be cooler in the PROG1 and PROG2 experiments than in the CONTROL1 experiments. Figure 3.2.2 shows reduced biases in meridional wind at 850hPa, particularly over the Arabian Sea for both PROG1 and PROG2 experiments with respect to CONTROL1. In this area meridional winds are usually over-estimated by the ECMWF's model as a result of an overly strong Walker circulation. Wind biases in East Asia are reduced of approximately 1-2 m/s. Likewise we observe a reduction in bias in the Southern Pacific, particularly off the coast of Peru. Change in wind biases close to Antarctica show an increase with respect to CONTROL1. However, we notice again that fewer grid points are actually contributing to that signal. Precipitation biases are also reduced over several Tropical regions, the Tibetan plateau and the North Pacific as shown in figure 3.2.3. Particularly interesting is the bias reduction in East Asia which amounts to 0.5-1 mm/day. Scorecards for the PROG1 and PROG2 experiments as compared to the CONTROL1 and CONTROL2 runs are shown in figures 3.2.4 and 3.2.5. Scorecards show the difference in Ranked Probabilistic skill between two experiments for 20 different parameter's (upper air and surface fields) weekly means (week 1: day 5-11, week 2: day 12-18, week 3: day 19-25 and week 4: day 26-32) over the Northern Extra-Tropics (north of 30N) and the Tropics (30N-30S band). Yellow and red colors (blue and cyan) colours indicate that the experiment being scored has lower (higher) RPSS than the control experiment. The higher the RPSS the more skillful the experiment is. A statistical test has been applied to the differences of RPSS scores. It is based on a 10,000 re-sampling bootstrap procedure. Dark blue and dark red dots indicate the difference of RPSS is statistically significant within the 5% level of confidence.

Both PROG1 and PROG2 experiments have a good performance with respect to the CONTROL1 experiment in terms of a number of variables, particularly in the Northern Hemisphere. Of particular relevance are the significant positive changes in experiment PROG2 for the Northern Hemisphere in meridional and zonal winds at 200 hPa as well as temperature at the same pressure level. Positive, significant changes are observed in experiment PROG2 also in meridional wind at 500 hPa, temperature at 850hPa and surface temperature. Positive, non-significant changes occur in most variables at all ranges. The Tropics show less of a response to the prognostic aerosols. It is interesting to observe that most of the significant impact occurs at the extended range (week 4)

which confirms the initial working hypothesis of a cumulative effect of the aerosol forcing over an extended time period. With respect to CONTROL2, PROG1 and PROG2 perform in a similar way with over positive impact even though the number of statistically significant improvements are less marked (see figure 3.2.5). Overall the performance of PROG2 remains more positive than that of PROG1. In general, the experiments with the radiatively interactive aerosols outperform the control experiments with the climatology.

Differences between the two experiments with prognostic aerosols (PROG1 and PROG2) can be ascribed to the different initializations. PROG1 was initialized with CAMSira whereas PROG2 was initialized with a climatology derived from a free-running model run with a recent version of the CAMS system. The climatology from the free-running model has more similar aerosol distribution to that of the interactive aerosol runs, given that both are free-running and have no observational constraint. On the contrary, the aerosol distribution in the interim reanalysis run is quite different, particularly for the dust aerosols, due to the use of a previous model version and the assimilation of aerosol optical depth from satellite observations. When using the CAMSira data for initialization, the EPS with interactive aerosols receives an initial "shock" being pushed away from its natural state. After a few days the impact of the initialization is felt less and both runs relax to a similar aerosol state. This is the possible cause of the better scores in the PROG2 run with respect to PROG1.

Specific plots and scores were produced for the West Africa (WA) region (10W-10E, 0-15N). These are shown in figures 3.2.6 and 3.2.7, only considering the PROG2 (gqm0) experiment with respect to the CONTROL1 (glqm) experiment. Specifically for WA, the largest impact is seen in velocity potential with a reduction in bias of up to 20 m^2/s in the experiment with the interactive aerosols at week 4. For a start date of May 1, this corresponds to the beginning of June which is in the pre-onset phase of the African Monsoon. Since velocity potential is considered a proxy for convection and MJO activity, a change in velocity potential can be relevant for the role of the MJO in the onset and intra-seasonal variability during the monsoon The scorecard calculated for the WA region (Figure 3.2.6) also show significant improvement in the upper level winds over the whole monthly range. The impact of prognostic interactive aerosols in the WA monsoon will be investigated further. In particular the role of biomass burning from Central Africa will also be investigated with sensitivity experiments.
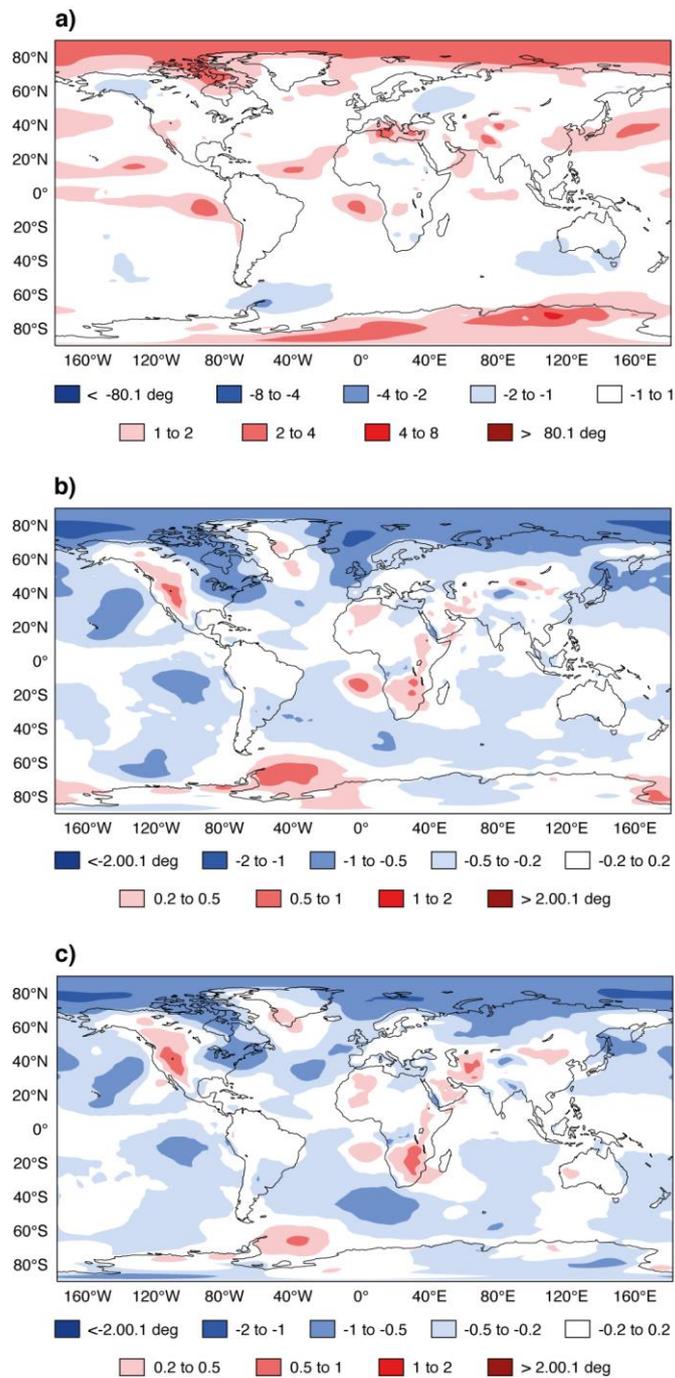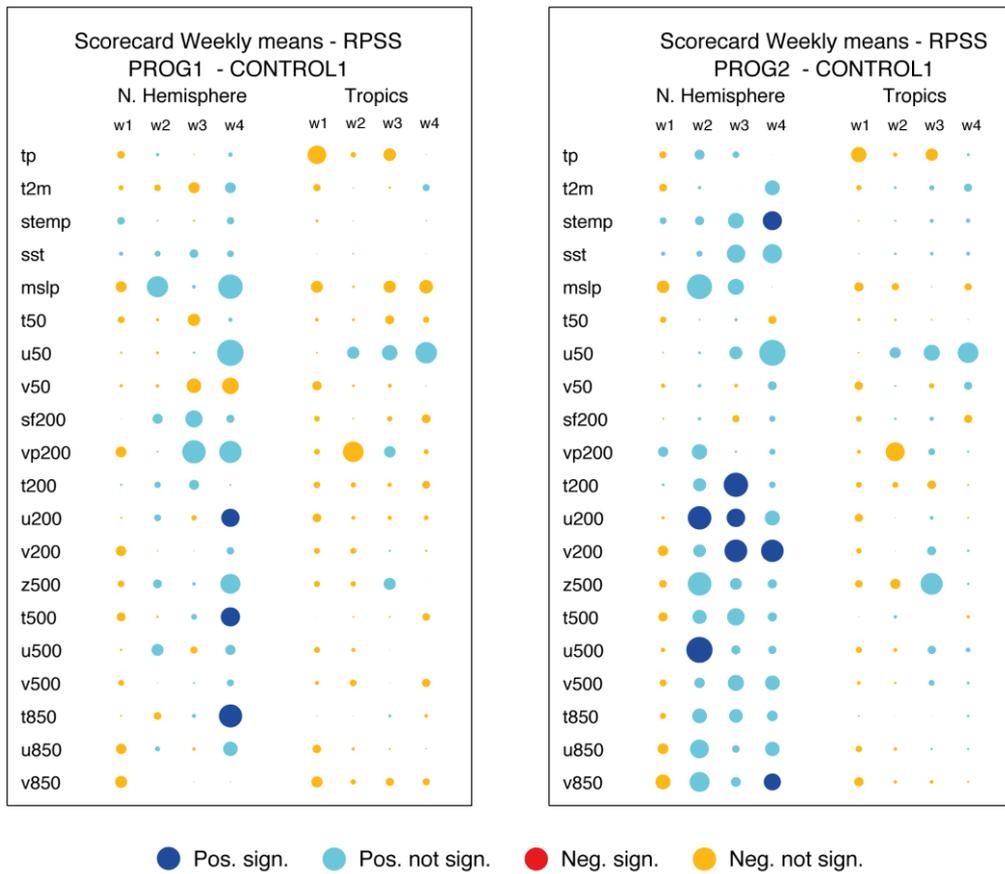
Figure 3.2.1: Bias in temperature (K) at 850hPa for CONTROL1 (a) at week 4 (end of May/beginning of June). Changes in bias (K) for PROG1-CONTROL1 and PROG2-CONTROL1 experiments, are shown in panels (b) and (c) respectively.
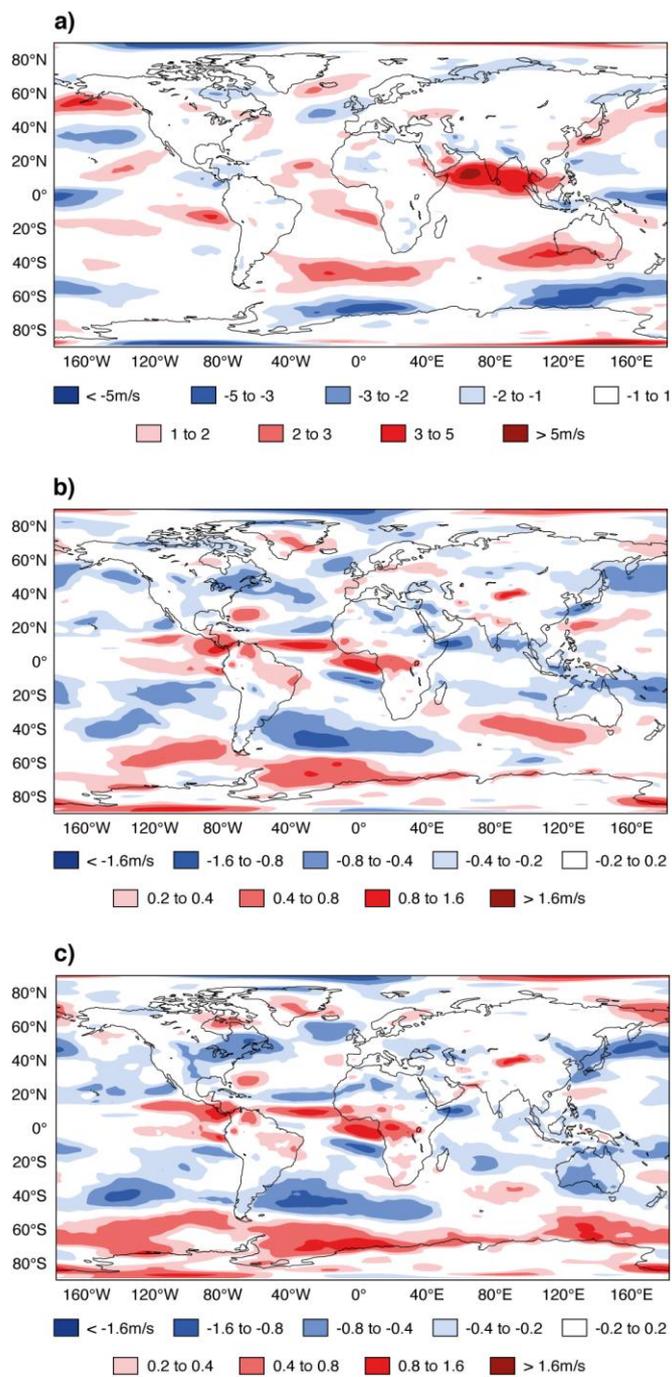
Figure 3.2.2: Same as in figure 1 but for meridional wind (m/s) at 850hPa.
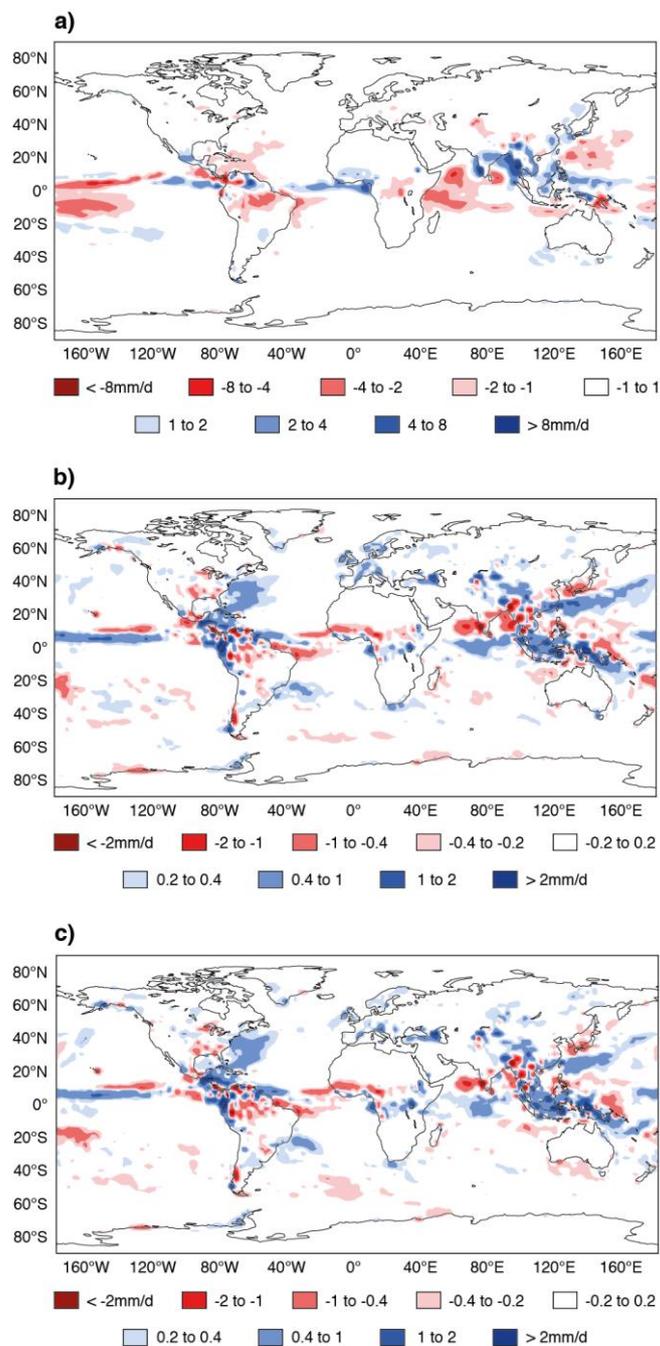
Figure 3.2.3: Same as in figure 1 but for total precipitation (mm/day).

Figure 3.2.4: Scorecards for experiments PROG1 (left) and PROG2 (right) compared to CONTROL1. The abbreviation w1 corresponds to week1 (5-11 days); w2 corresponds to week2 (12-18 days), w3 corresponds to week3 (19-25 days) and w4 corresponds to week 4 (26-32 days) from the start date (May 1). The following variables are verified: total precipitation (tp), 2m temperature (t2m), surface temperature (stemp), sea surface temperature (sst), mean sea level pressure (mslp), temperature at 50 hPa (t50), horizontal wind at 50 hPa (u50), meridional wind at 50 hPa (v50), streamfunction at 200 hPa (sf200), velocity potential at 200 hPa (vp200), temperature at 200 hPa (t200), horizontal wind at 200 hPa (u200), meridional wind at 200 hPa (v200), geopotential at 500 hPa (z500), temperature at 500 hPa (t500), horizontal wind at 500 hPa (u500), meridional wind at 500 hPa (v500), temperature at 850 hPa (t850), horizontal wind at 850 hPa (u850), and meridional wind at 850 hPa (v850). See text for an explanation of the verification metrics.
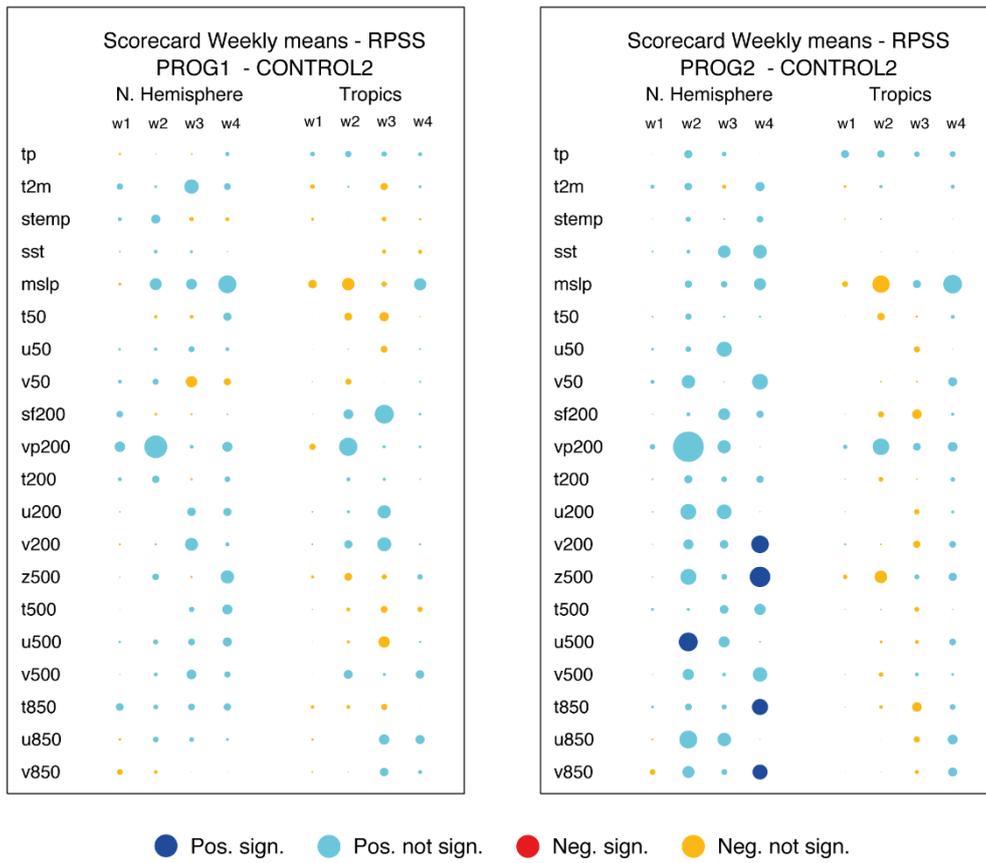
Figure 3.2.5: Scorecards for experiments PROG1 (left) and PROG2 (right) compared to CONTROL2
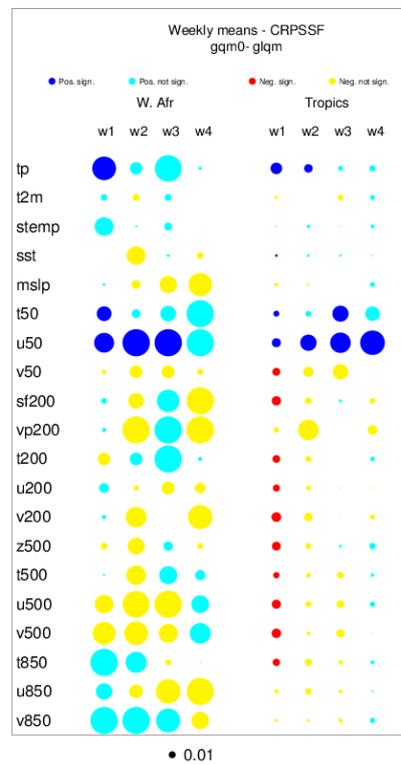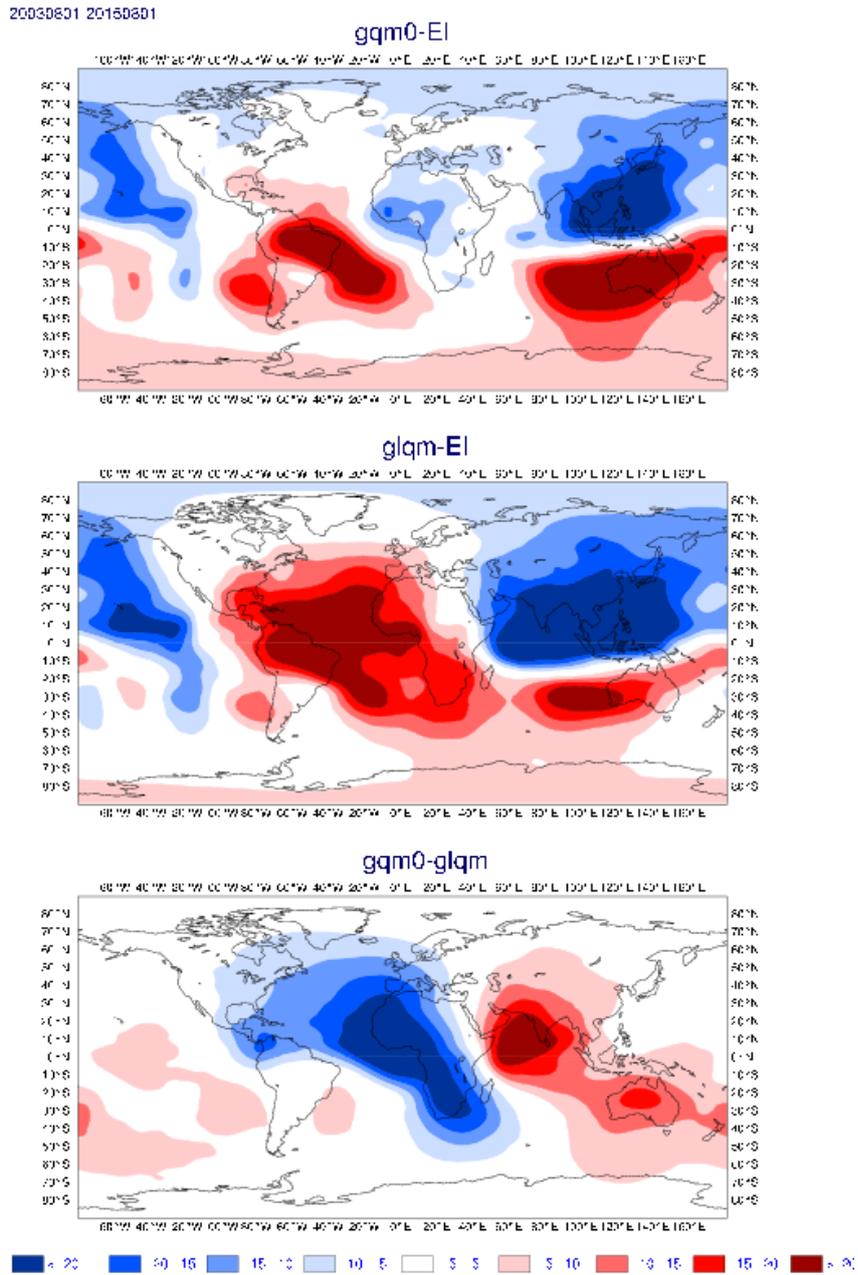

Figure 3.2.6: Scorecard for experiments PROG2 compared to CONTROL1 over the West Africa region.

Figure 3.2.7: Bias in velocity potential at week 4 (beginning of June) for PROG2 experiment (top panel, gqm0) and CONTROL1 experiment (middle panel, glqm). Bottom panel shows the difference between PROG2 and CONTROL1.

3.3   WRF-CHIMERE analysis (UPMC)

The first evaluation is presented by comparing the aircraft measurements to the model outputs. In order to superimpose the measurements and the model, the model outputs are spatially and temporally interpolated at the place and exact time of the measurements. We focus on pollutant transport from the Guinean coast at Lomé (Togo) toward the DACCIWA super-site at Savé (Benin) on 5 July.Results are presented for the aerosol in Figure 3.3.1 and for the meteorological variables in Figure 3.3.2.

Aerosol evaluation

For the aerosol, the modeled species are compared to the measured ones: Black Carbon (BC), Organic Carbon (OC), sulfate, nitrate and ammonia in Figure 3.3.1. For the ATR and Falcon flights the altitude of the measurements evolves between 0 and 2000m above ground level (for black carbon, there is no measurements for this specific flight). *As expected for aerosol concentrations, the impact of the aerosol effect is lower than the impact of the emissions scenario. The comparison of no AE-HTAPx10 and AE-HTAPx10 shows differences lower than +/-0.1 ug/m3 for OC and BC. These results show that the use of aerosol effect in WRF-CHIMERE could change BC and OC concentrations of less than 10% during these two flights.*

For black carbon, there are no measurements for this specific flight. But the model to model comparison shows that the increase of HTAP emissions leads to an increase in concentrations with some local peaks mainly when the aircraft is close to the surface, in the surface layer where pollutants are less vertically mixed than in the convective boundary layer. *Regarding BC and OC, the AE-HTAP simulation gives relatively constant concentrations, around 0.5 ug/m3 (Figure 3.3.1). When the emissions are multiplied by ten (with AE-HTAPx10 and noAE-HTAPx10), concentrations are higher and with a large variability during the flight. In this case, the concentrations are varying between 0.5 and 3 (for BC) to 6 ug/m3 (for OC).* For OC, the model configuration with HTAPx10 enabls to have better comprison to the measurements than with the regtular HTAP fluxes. The concentrations with and without the indirect effects shows low differences and the model results remain far from the measured values. *As expected for aerosol concentrations, the impact of the aerosol effect is lower than the impact of the emissions scenario. The comparison of no AE-HTAPx10 and AE-HTAPx10 shows differences lower than +/-0.1 ug/m3 for OC and BC. These results show that the use of aerosol effect in WRF-CHIMERE changes BC and OC concentrations by less than 10% during these two flights.* For the inorganic species (nitrate, ammonia and sulfate) the simulations are not able to provide correct concentrations compared to the measurements, except for Ammonia. The variability due to the fact to take into account the indirect effect is non negligible but is not the reason of the bias between model and observations. There is probably a problem with the emissions inventory used, the speciation of the emitted species, independent of the model coupling. For the Falcon measurements, the recorded concentrations of inorganic species are zero before 12:20 UTC which seems unrealistic. After, when measurements are available and seem realistic, the model is not able to catch the measured values.
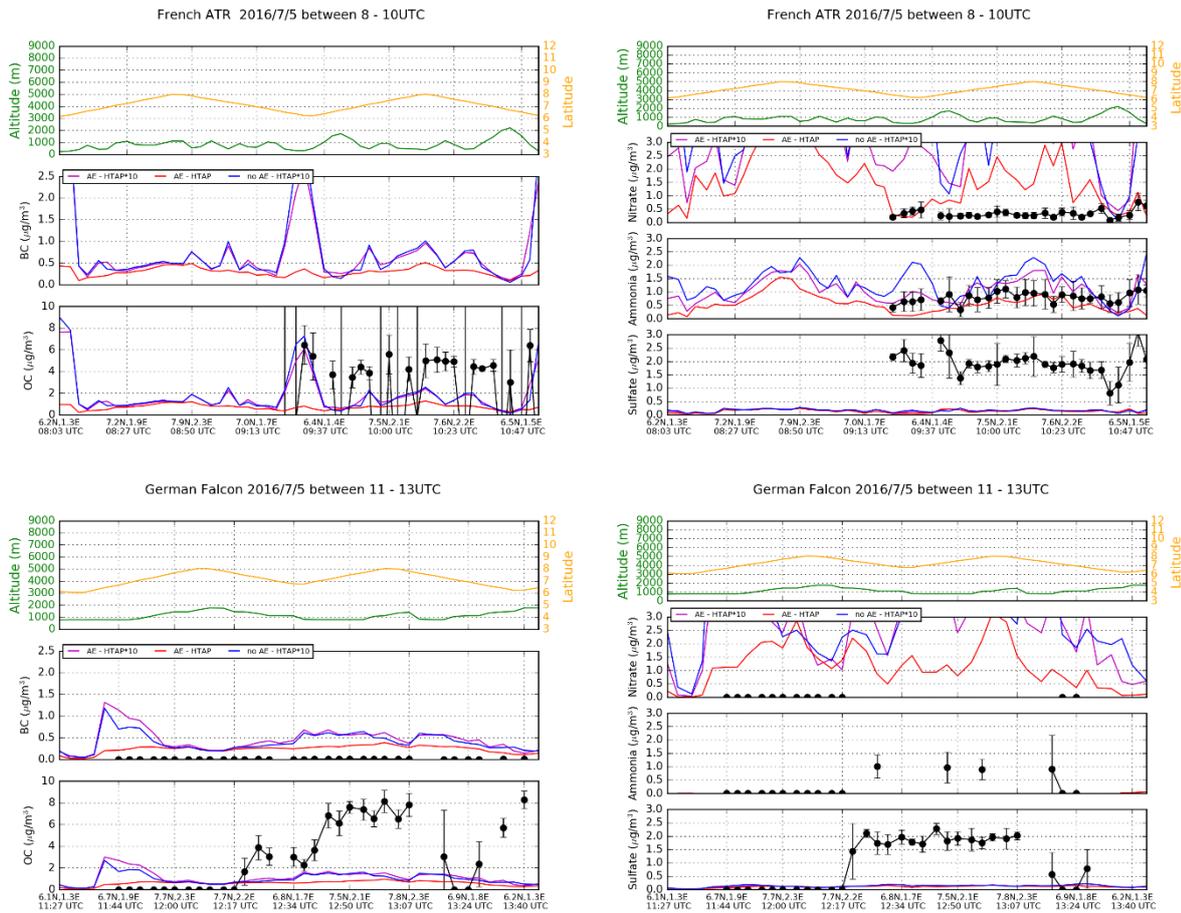
Figure 3.3.1: Time series comparing on 5 July 2016 measurements made by the French research ATR42 aircraft operated by the SAFIRE team (top) and by the German research Falcon aircraft operated by the DLR team (bottom) with WRF-CHIMERE modeled fields of the CHIMERE model. The altitude (in m asl) and the latitude (in °N), black carbon concentration (BC in µg.m-3), organic carbon concentration (OC in µg.m-3), nitrate concentration (in µg.m-3), ammonia concentration (in µg.m-3) and sulfate concentration (in µg.m-3). Raw airborne observations at 1 Hz are averaged every 3 minutes (black dots) and the 4D modeled fields are interpolated along the flight trajectory every 3 minutes for three simulations: (i) without Aerosol Effect and HTAP anthropogenic emission multiplied by 10 (no AE – HTAP x10), (ii) with AE and HTAP standard (AE – HTAP), (iii) with AE and HTAP anthropogenic emission multiplied by 10 (AE – HTAP x10).

Meteorology

Figure 3.3.2 presents the same type of comparison as Figure 3.3.1 but for the thermodynamic meteorological variables. The goal of this comparison is to see if the discrepancies analyzed for the chemical species are due to meteorological biases or not. Globally, the model is good for the modeling of the meteorological variables and for the two flights measurements. *Regarding meteorological variables (Figure 3.3.2), the two simulations with aerosol effects (AE-HTAPx10 and AE-HTAP) are identical (the purple line is under the red line), which shows that the larger amount of aerosol in AE-HTAPx10 compared with AE-HTAP has no impact during this day. But these two simulations presents some differences with the noAE simulation. There is a difference on the meteorology with ~+/-1m/s for the wind speed, ~+/-5% for the relative humidity and ~ +/- 1K for the temperature. On 5 July, aerosol effects have a limited impact on meteorology, which is logical because this day is cloudy with a moderate wind.*
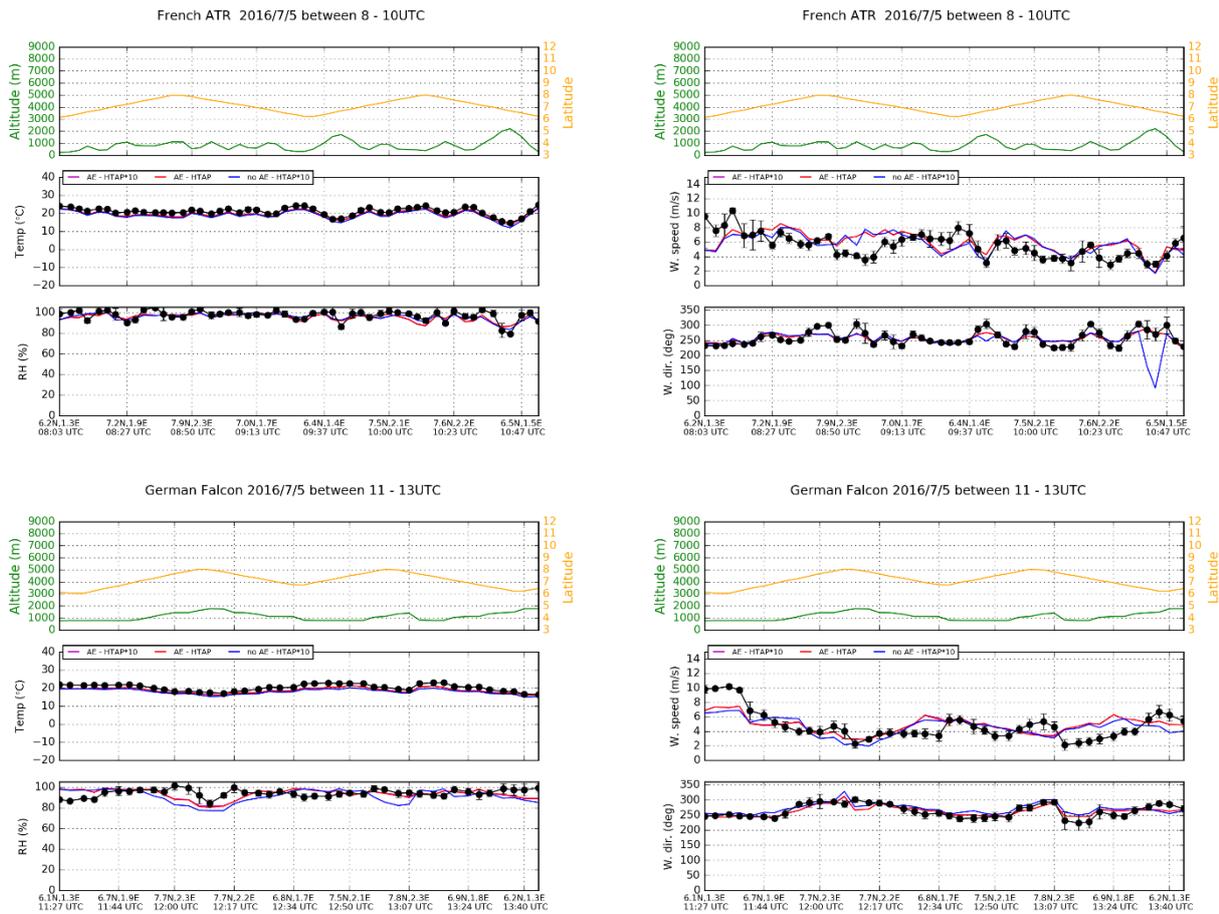
Figure 3.3.2: Time series comparing on 5 July 2016 measurements made by the French research ATR42 aircraft operated by the SAFIRE team (top) and by the German research Falcon aircraft operated by the DLR team (bottom) with WRF-CHIMERE modeled fields of the CHIMERE model. The altitude (in m asl) and the latitude (in °N), temperature (in Celsius), relative humidity (RH in %), wind direction (in degree) and speed (in m.s-1). Raw airborne observations at 1 Hz are averaged every 3 minutes (black dots) and the 4D modeled fields are interpolated along the flight trajectory every 3 minutes for three simulations: (i) without Aerosol Effect and HTAP anthropogenic emission multiplied by 10 (no AE – HTAP x10), (ii) with AE and HTAP standard (AE – HTAP), (iii) with AE and HTAP anthropogenic emission multiplied by 10 (AE – HTAP x10).

The comparison for the meteorological data mainly shows that there is overall a good agreement between observation and modeling. The temperature is very well reproduced for all three simulations and the relative humidity is slightly improved with the aerosol effect. The wind speed range is in good agreement and the altitude of the wind sher is improved.

In conclusion, these comparisons showed that the model discrepancies are not due to the meteorological modeling but probably to the anthropogenic emissions used. For the chemical concentrations, the contribution of the aerosol indirect effect is visible but not really important on the concentrations.

Regional modelling of clouds and aerosol interactions across the SWA

In order to assess aerosol and cloud interactions, we focus on 5 July 2016 which was a cloudy day over SWA. We compare observations with three simulations in order to analyze the sensitivity of the model. First we compare modelling against aircraft measurements of aerosols distribution
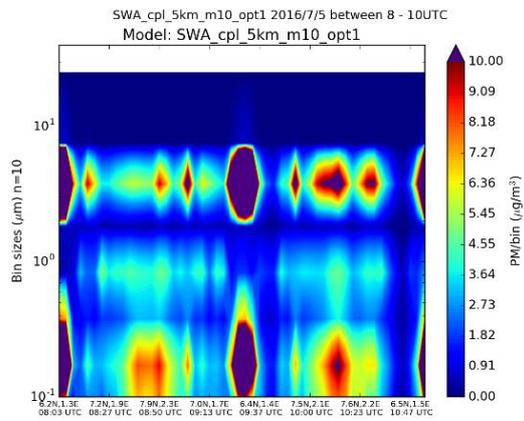
Aerosol regional level

We use the measurements of the Optical Particle Counter (OPC) in order to evaluate the modeled regional aerosol distribution in mass.
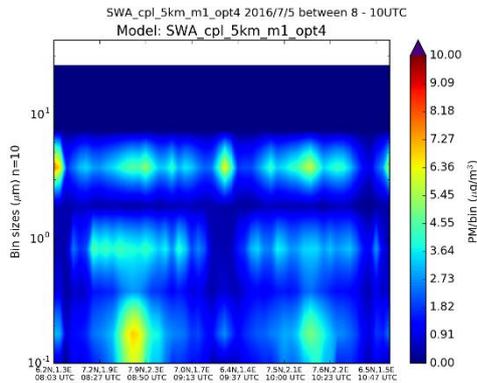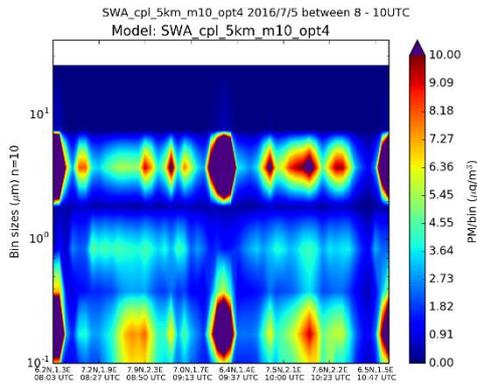
1) Aircraft – OPC
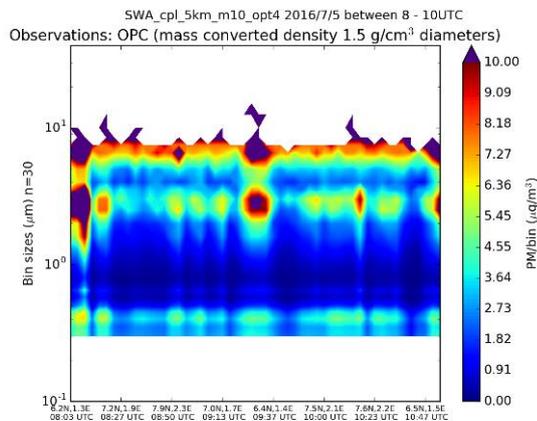
2) CHIMERE – no AE – HTAP x10

3) CHIMERE – AE – HTAP

4) CHIMERE – no AE – HTAP x10

Figure 3.3.3: Aerosol mass distribution (per bin size) measured (1st panel) and observed (panels 2, 3 and 4) along the ATR flight trajectory on 5 July 2016. The WRF-CHIMERE modeled fields corresponds to three simulations: (i) without Aerosol Effect and HTAP anthropogenic emission multiplied by 10 (no AE – HTAP x10), (ii) with AE and HTAP standard (AE – HTAP), (iii) with AE and HTAP anthropogenic emission multiplied by 10 (AE – HTAP x10). Modeled PBL height is the violet dashed line.

Regarding the aerosol mass distribution, observations made by the OPC instrument onboard the ATR shows (Figure 3.3.3) that this is composed of three modes fine at 100 nm, intermediate at 1 µm and coarse at 5 µm. The highest values are noticed close to the coast where high density population is located.The modeled distribution with the standard HTAP emission clearly underestimates the observations. With HTAP emission multiplied by 10, the aerosol mass distribution appears more realistic.

3.4 Met Office Unified Model analysis (Leeds and Met Office)

This aim of this work is to evalue the Unified Model (UM) to determine whether it is an appropriate tool to assess the sensitivity of the cloud field to aerosol. The sensitivity work is reported on in D4.4 using an additional cloud microphysics module known as CASIM. Here we assess the UM without the CASIM module as a baseline test.

It is important that the UM is able to generate the appropriate stratocumulus cloud which we expect to be sensitive to aerosol and it is important that deep convection is represented in a realistic way. However, the stochastic nature of deep convection means that we do not expect individual storms to be represented within the simulations, but a good result will be that deep convective systems form in similar regions with a similar diurnal cycle and have a similar lifetime and propagation direction and speed.

The following series of maps show the longwave (lw) and shortwave (sw) top-of-atmosphere (TOA) radiative flux from the simulation on the left panels and the SEVIRI false colour dust product generated from satellite measured infrared radiation. The intention is to use these images to simply identify stratocumulus cloud and deep convection. Deep convection is visible as bright regions in the simulation lw field as well as in the daytime sw field. It is visible as red and black regions in the SEVIRI imagery. Stratocumulus is visible during the daytime in the sw field and shows some structure in the lw field in some cases. The simulations begin at 0000 UTC on the 10th of July (Figure 3.4.1). The initial panel shows the initialisation field regridded from the driving global model. On this panel it can be seen that the deep convection visible in the SEVIRI imagery is not shown on the simulation. This is because the convective parameterisation used in the global driving model is known to not effectively generate large propagating systems as seen in the imagery.

By midday (Figure 3.4.2) the fine scale structure in the simulations has spun up in the simulation. Stratocumulus cloud can be seen over the ocean with cloud over the continent south of 11-14°. Deep convection has formed at the west coast. In the SEVIRI imagery there is little stratocumulus because the region has been disrupted by the passing through of a mesoscale convective system that initiated the previous day. Instead there are shreds of high and medium cloud. The simulation did not have this system the previous day, therefore it is not surprising that the simulation did not present the same situation.By 1800 on 10th July deep convection is initiating in the simulation over Nigeria and similar sytstems are forming in the SEVIRI imagery (Figure 3.4.3). In the SEVIRI imagery a string of smaller systems is forming across the region on the northern borders of Ghana, Togo and Benin. These systems are not captured by the simulation. However the convection further west is captured by the simulation.

By 0000 on the 11th July, the convection to the west and east of the domains are the dominant features on both the simulation and SEVERI imagery (Figure 3.4.4). To the east the simulation has a little more high cloud than the SEVIRI imagery, however this region is close to the domain boundary and influenced by deep convection off the east edge of the domain which will not be captured by the global driving model. Hence this discrepancy in intensity is not surprising.

By 1200 on 11th July we have a much more typical situation (Figure 3.4.5). Stratocumulus is clear in the simulation and SEVIRI imagery over much of the DACCIWA region. The model is also capturing deep convective systems on the west coast and over Nigeria. By 1800 on the 11th the model captures the deep convection forming at the northern extent of the stratocumulus on the north border of Ivory Coast. It also captures the deep convection occurring over Nigeria later in the day (not shown). In both the model and the simulation these systems aggregate as we reach 0000 on 12th of July (Figure 3.4.6) and are dissipating by 0600 on 12th July (not shown).

By 1200 on 12th July we return to a state with stratocumulus cloud over much of the DACCIWA region of interest with remnants of deep convection at the west coast (Figure 3.4.7). The simulation captures both the stratocumulus and the high cloud. By 1800 on 12th July New deep convection is initiating in Nigeria and Niger in the SEVIRI imagery (Figure 3.4.8). This exists in the simulation but is perhaps over a smaller area and slightly further west.

In summary, we find that after 1 day spin up, the Unified Model run at 4.4 km resolution is capable of producing stratocumulus over the DACCIWA region during the day. It is capable of producing deep convection in the evening in regions which agree with the SEVIRI imagery within approximately 100 km. This includes mesoscale convective systems initiating in Nigeria and propagating to the west and smaller systems initiating on the northern edge of the stratocumulus and aggregating to form larger systems. As a result, we find that the Unified Model operated at this resolution is a useful tool for forecasting and for use in scientific and sensitivity studies related to cloud during this period.
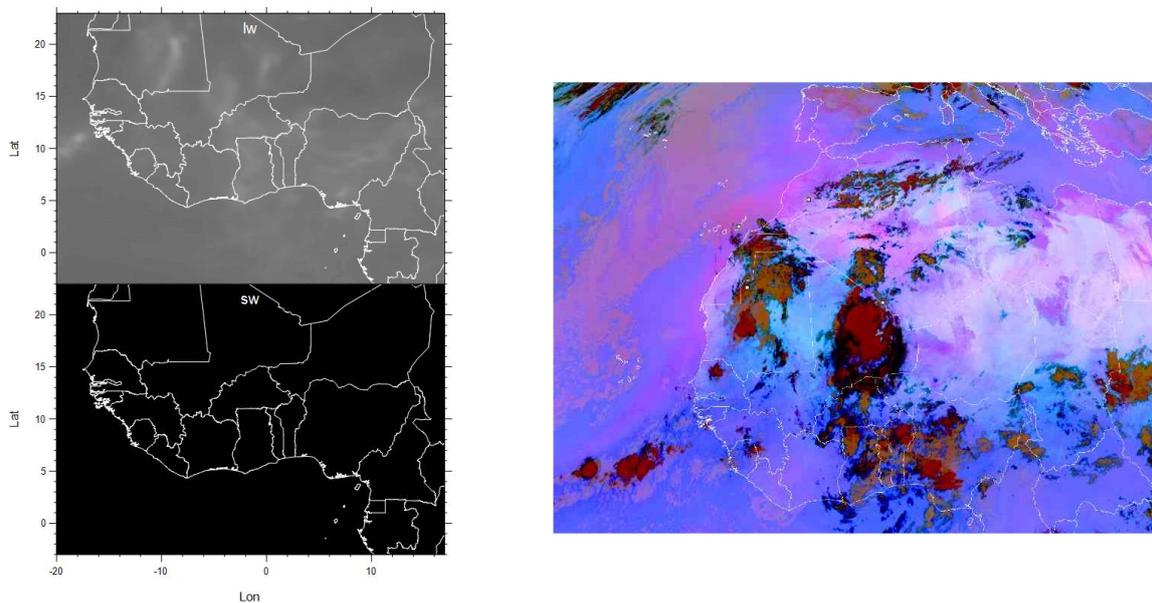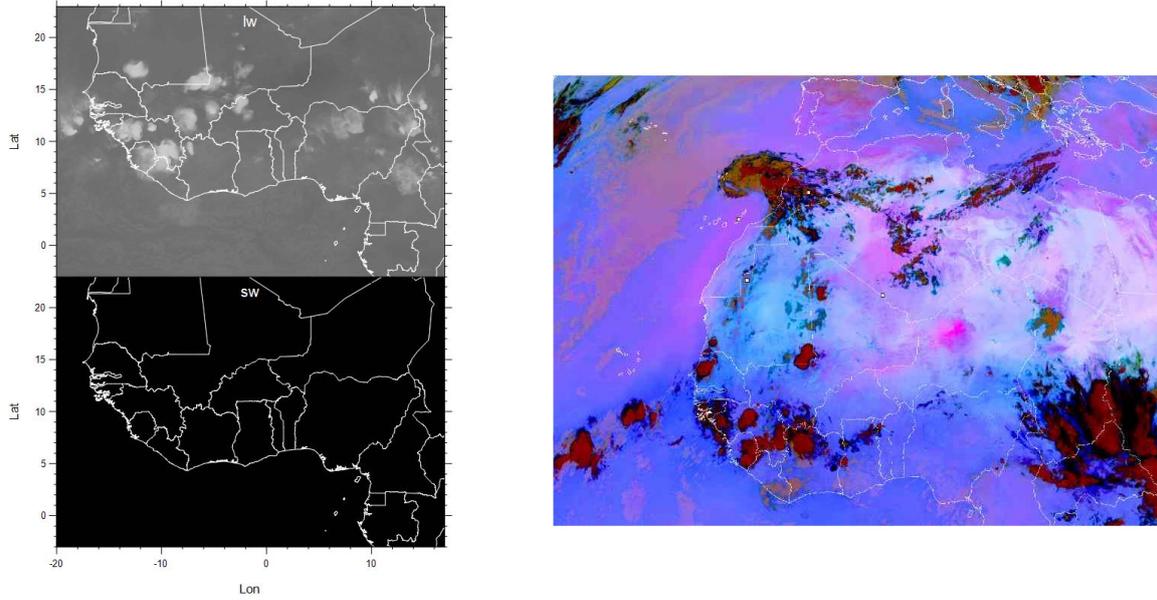

Figure 3.4.1: 10th July 2014 0000 UTC T+00. Left shows modelled TOA longwave (lw) and shortwave (sw). Right. shows SEVIRI false colour longwave imagery (see text for details)
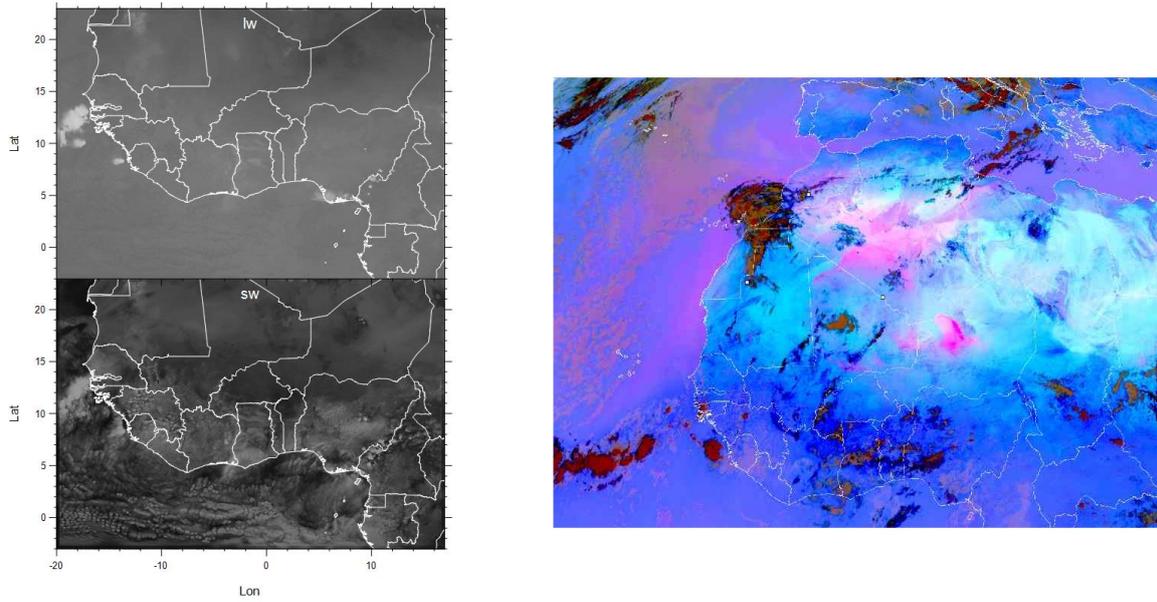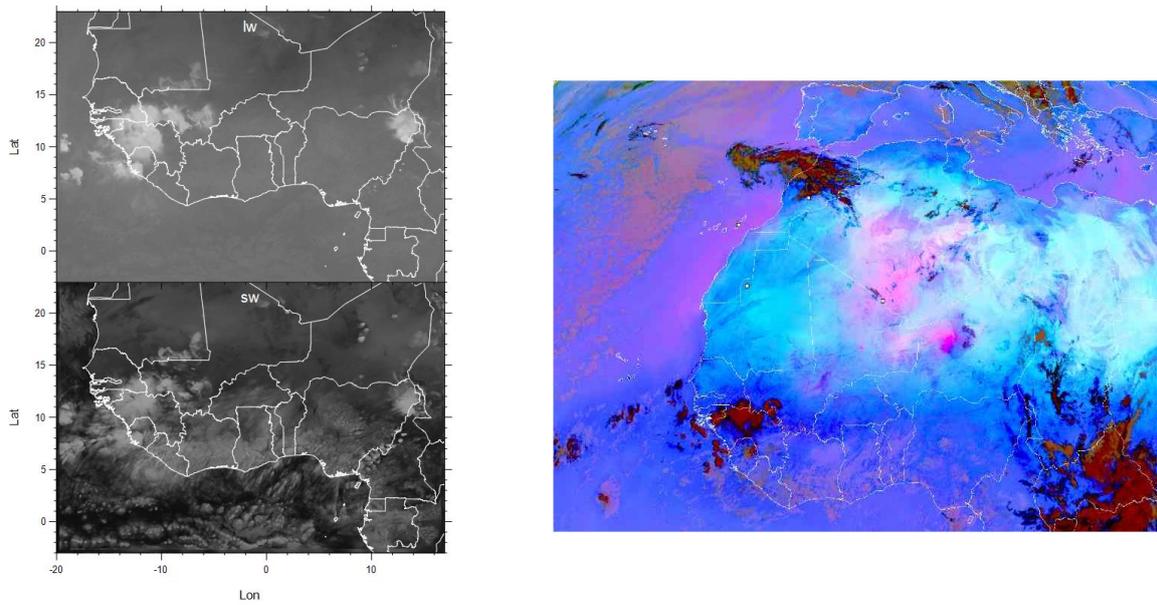
Figure 3.4.2: As Figure 3.4.1, but 10th July 2014 1200 UTC T+12
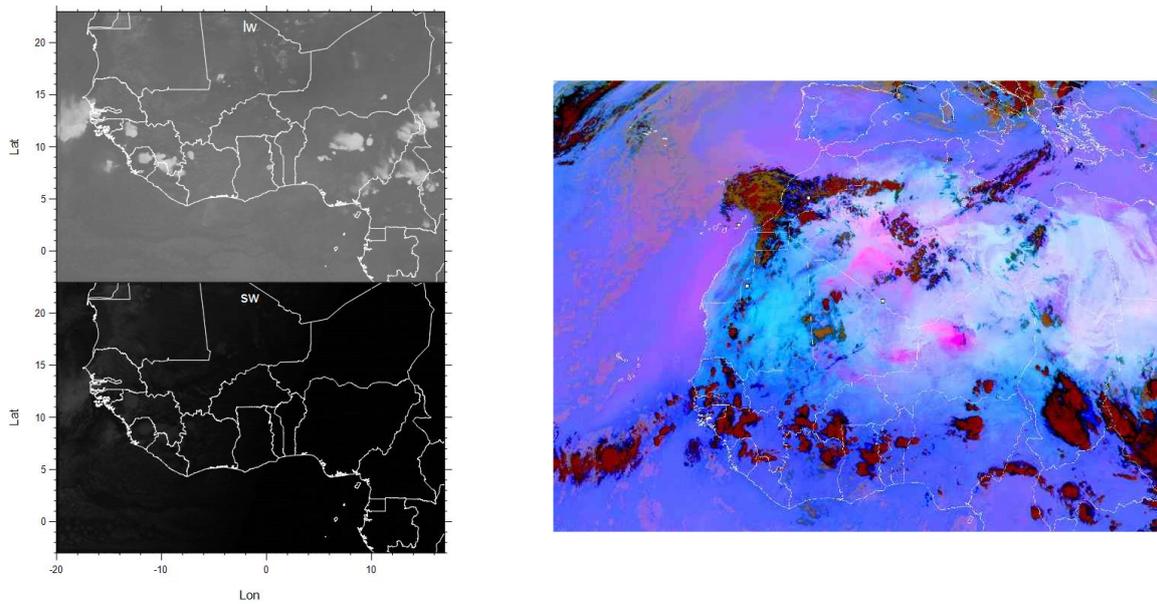
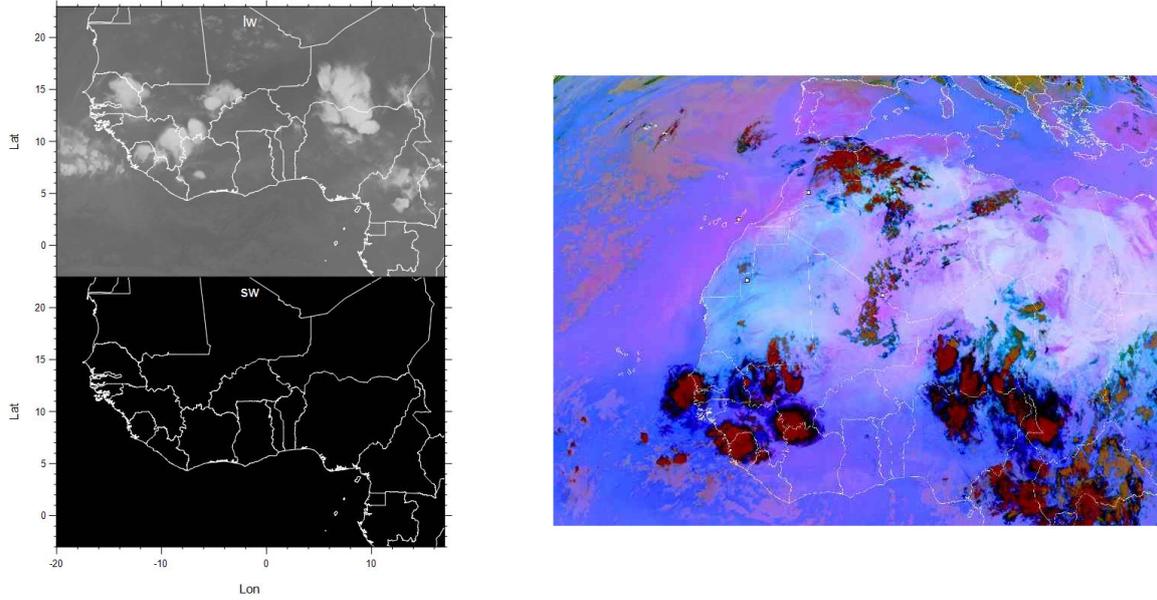

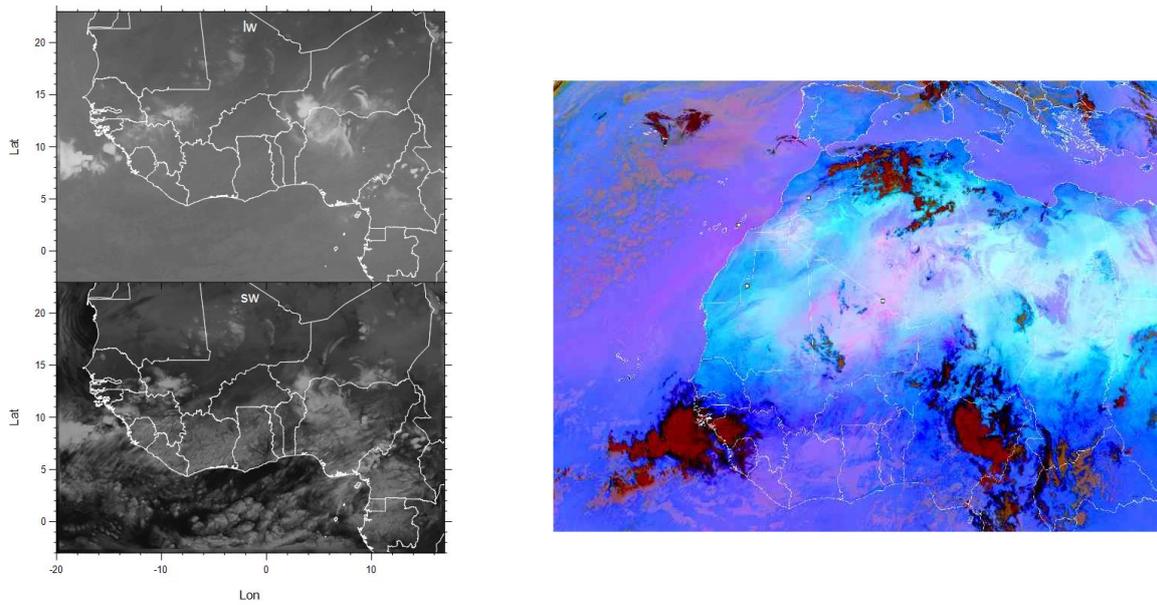*Figure 3.4.3: As Figure 3.4.1, but 10th July 2014 1800 UTC T+18*

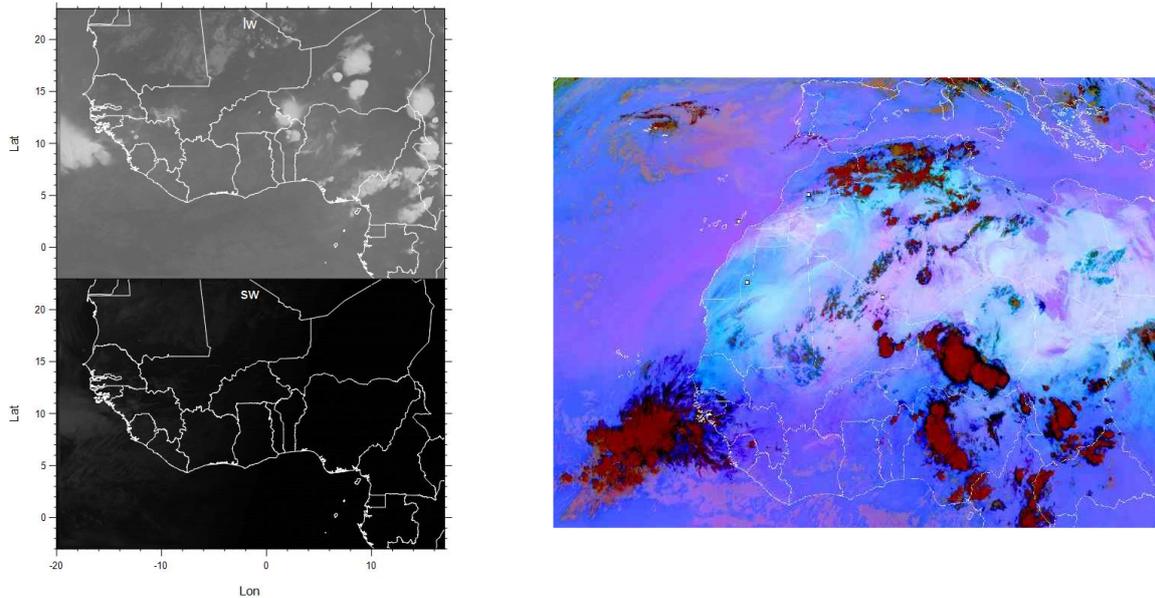*Figure 3.4.4: As Figure 3.4.1, but 11th July 2014 0000 UTC T+24*

Figure 3.4.5: As Figure 3.4.1, but 11th July 2014 1200 UTC T+36

Figure 3.4.6: As Figure 3.4.1, but 12th July 2014 0000 UTC T+48


*Figure 3.4.7: As Figure 3.4.1, but 12th July 2014 1200 UTC T+60*

Figure 3.4.8: As Figure 3.4.1, but 12th July 2014 1800 UTC T+66

3.5   COSMO-ART analysis (KIT)

To evaluate the modeled cloud properties, observations of the research aircraft British Antarctic Survey (BAS) Twin Otter on 3 July 2016 between 10:47 UTC and 14:06 UTC (flight number TO-02) are used, capturing the Lomé-Savè area. The following figures show the flight path and altitude (Fig. 3.5.1) as well as the observed and modeled cloud droplet number concentration (CDNC, Fig. 4.8a,b) and effective radii (Fig. 3.5.2 c,d). The aircraft position between 10:45–11:30 UTC, 11:30–12:30 UTC, 12:30–13:30 UTC and 13:30–14:06 UTC is shown in blue, grey, red and black, respectively, for the flight track (Fig. 3.5.1a) and the altitude (Fig. 3.5.1b). For a more robust statistical comparison of the observed and modeled cloud location, the comparison with COSMO-ART is not realized along the flight track but by using the cubes that are spanned horizontally by the rectangles around the flight track sections for 11-14 UTC (according to the hourly output of COSMO-ART) and vertically by the lowest 2.3 km AGL in accordance to the Twin Otter maximum flight altitude during this flight. The observed and modeled CDNC and effective radii are compared via boxplots (Fig. 3.5.2) for the flight track sections at 2 July between 11 UTC and 14 UTC. The boxplot colors follow the definition in Figure 3.5.1. For 11 UTC, the observations are omitted since the Twin Otter did not penetrate clouds during that time. The modeled CDNC (Fig. 3.5.2b) are generally higher than the observed ones (Fig. 3.5.2b) but both stay below a median of 400 cm^{-3}. The model shows a general trend of increasing median CDNC with time. This is expected during the SCT, since cumulus clouds tend to have a higher CDNC than stratus.
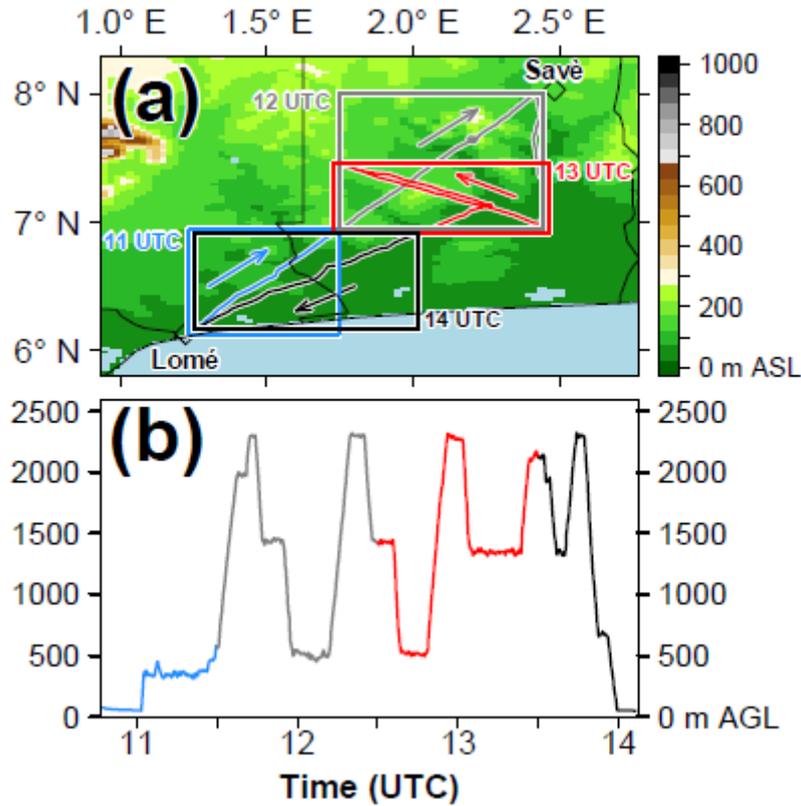
Figure 3.5.1: Flight track of the Twin Otter aircraft on 3 July 2016 between 10:47 UTC and 14:06 UTC (flight number TO-02) in (a) horizontal and (b) vertical dimension (m AGL). For (a) the topography (m ASL) is added. The flight track in (a) and (b) is separated in hourly time steps for the subsequent collocation with hourly model data from COSMO-ART, highlighted by the blue (10:47–11:30 UTC), gray (11:30–12:30 UTC), red (12:30–13:30 UTC) and black color (13:30–14:06 UTC). The rectangles, spanned by the horizontal extension of the hourly flight sections, are used for the selection of model data. Furthermore, the arrows in (a) indicate the flight direction with the takeoff at Lomé, the flight to Savè and the return to Lomé airport. Shortly after 12 UTC (with a flight altitude of 0.5 km AGL) the Twin Otter reached Savè. Note the meridional compression of the map in (a).
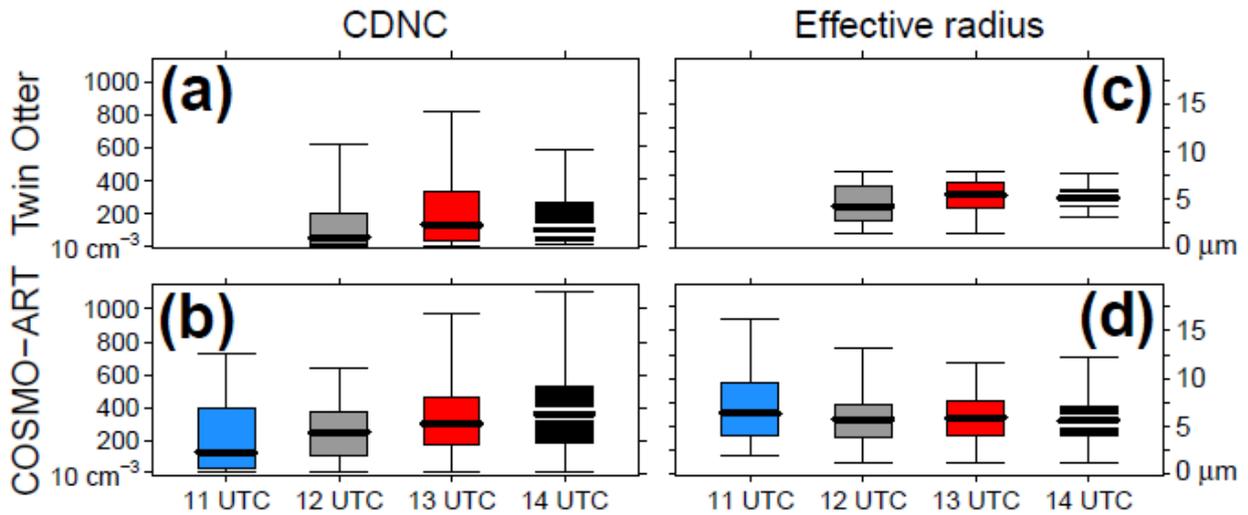
Figure 3.5.2: Boxplots of (left) the CDNC (cm-3) and (right) the cloud droplet effective radius (µm) according to the flight track denoted in Figure 3a for (top) Twin Otter observations and (bottom) COSMO-ART reference case. The flight track is separated in hourly time steps from 11 UTC to 14 UTC as highlighted by the colors (compare Fig. 3). Regarding (a,c) the observations according to the flight track section with 1 s temporal resolution of the CDP device are used. Regarding (b,d) the simulation results of the cube that is spanned horizontally by the rectangles in Figure 3a and vertically about 2.3 km (in agreement with the Twin Otter maximum flight altitude) are considered. The whiskers capture the data from the 0.025 to the 0.975 quantile (95% of the data). Data outside this range are not shown. CDNC below 10 cm-3 were omitted, leading to an observational data basis of 34, 443, 403 and 115 observations at 11, 12, 13 and 14 UTC, respectively. Due to the low observational data coverage 11 UTC is omitted.

We used the COSMO-ART model to simulate the effect a large influx of biomass burning aerosol would have on cloud formation by carrying out two simulations for 6 July: one of which included biomass burning aerosol (FIRE) and one of which did not (NO FIRE). Figure 3.5.3 show two-dimensional histograms of cloud droplet number concentration and effective radius across the domain on this day. In the NO FIRE case, the number concentrations are lower and the effective radii higher than in the FIRE case. Over the marine domain (9°W-4.33°E, 3-4°N), the cloud droplet number concentration is 32.9% higher when the fires are switched on; over the whole domain (9°W-4.33°E, 3-10°N), it is 7.5% higher.
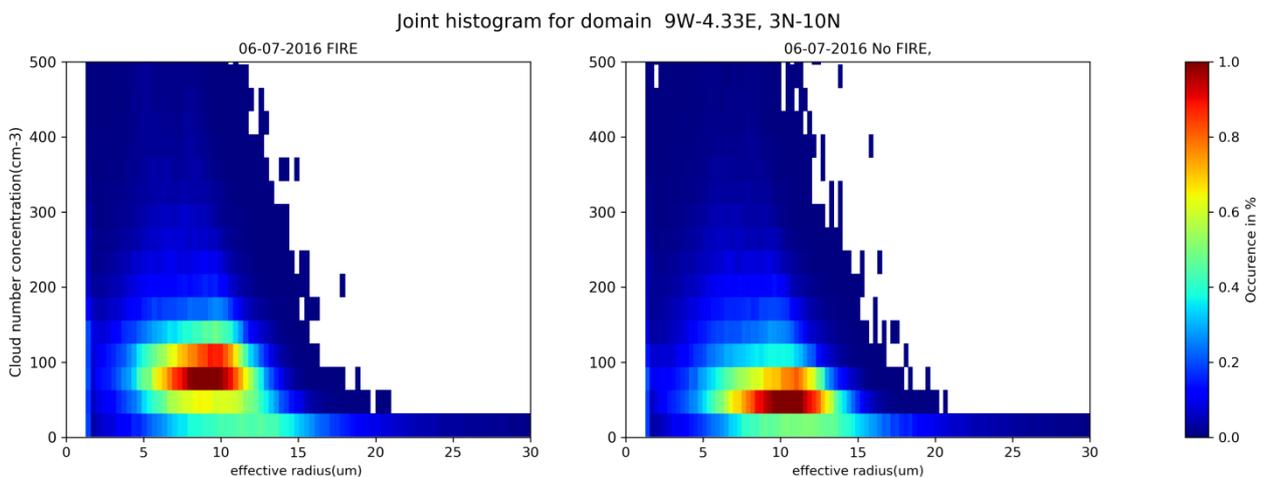
Figure 3.5.3: Two-dimensional histogram showing of the simulated cloud properties in the FIRE (left) and the NO FIRE (right) simulations.

In summary, a comparison of simulated cloud droplet number with observed ones shows a reasonable agreement although the simulated cloud droplet number concentrations are somewhat high. This could be an indication that the emission data might be too high as indicated by other findings not presented here. A quite interesting result that could not be expected previous to DACCIWA is the great importance of biomass burning aerosol for the cloud microphysical properties. The origin of the biomass burning aerosol is Central Africa and by long range transport impacts the cloud properties in the DACCIWA region.

4   Conclusions

Analysis under D4.5 spans clouds and aerosols on regional to global scales. High resolution Unified Model, COSMO-ART WRF-CHIMERE runs that explicitly capture deep convection (grid spacings of 4km and 5km) can in case studies capture both the stratus/stratocumulus and deep convection reasonably well, but global climate models (with grid spacings ~100km) have well established biases in both the thin low-level layer clouds and the deep convection.

There is evidence that prognostic interacting aerosols can improve the models. In WRF-CHIMERE, in general, runs with the radiatively interactive aerosols outperform runs using a climatology. Differences in the meteorology caused by using HTAP emissions multiplied by 10 rather than HTAP emissions are negligible and much smaller than differences caused by using aerosol effects or no aerosol. Similarly, in ECHAM, the amount of anthropogenic aerosol has a small effect on the clouds, since the clouds always have abundant aerosol to act as CCN, a result supported by process studies described in the D4.4 report. A similarly universal result across models that was not expected before DACCIWA is the importance of biomass burning for the cloud microphysical properties. The biomass burning aerosol originates from Central Africa and is transported into the DACCIWA. providing background pollution on which the local anthropogenic emissions are imposed.

In WRF-CHIMERE, for OC the model configuration with HTAPx10 enabls to have better comparison to the measurements than with the regtular HTAP fluxes. The concentrations with and without the aerosol effects shows low differences and the model results remain far from the measured values. Aerosol mass is also more realistic with HTAP emissions multiplied by 10. For nitrate and sulfate the simulations are not able to provide correct concentrations and aerosol effects are non negligible, but not the reason for the bias between model and observations, which is likely instead the emissions inventory used, rather than the modelled meterorology. In COSMO ART cloud droplet numbers are in reasonable agreement with observations, but slightly too high. This suggests that emissions in COSMO-ART are too high, which is also indicated by other findings not presented here.

In ECHAM the lowest near-surface aerosol concentration is surprsingly simulated in a run using prescribed biomass buring emissions that are three times higher than those in a run with the highest near-surface aerosol concentrations. This occurs as due to feedback mechanisms dust emissions are higher in the run with lower biomass burning emissions, highlighting the need to understand dust emission, transport and deposition processes to model aerosol even in southern West Africa. Another notable feedback is between aerosols, clouds and the Atlantic inflow to the West African monsoon itself have been investigated, showing aerosols slowing the front propagation of the inflow (see D4.4).

The most striking result for operational weather prediction is that ECMWf hindcasts on time-scales of upto 4 weeks are improved using direct effects from prognostic aerosols, rather than a climatology (although biomass burning emissions are unrealistiaccly accurate from an operational perspective as observed fires were used). Initialisation of the aerosols matters early in the period, and the small forcings from aerosols direct effects build up over time to give the largest effects at week 4. Over

West Africa, the bias in the velocity potential is reduced by up to 20 m^2/s in the experiment with the interactive aerosols at week 4, this may be relevant for the role of the MJO in monsoon onset and intra-seasonal variability during the monsoon Upper level winds are also significantly improved. These effects over West Africa will be investigated further, in particular the role of biomass burning aerosols from Central Africa.

5 References

Adler, B., Kalthoff, N., and Gantner, L., The life cycle of nocturnal low-level clouds over southern West Africa analysed using high-resolution simulations, Atmos. Chem- Phys., 2016, doi:10.5194/acp-2016-842.

Boucher, O., M. Pham, and C. Venkataraman, 2002: Simulation of the atmospheric sulfur cycle in the LMD GCM: Model description, model evaluation, and global and European budgets. Note 23, 26pp.

Bozzo, A., S. Remy, A. Benedetti, J. Flemming, P. Bechtold, M. Rodwell, and J.-J. Morcrette, 2017: Implementation of a cams-based aerosol climatology in the IFS. ECMW, Technical Memorandum 801.

Dee, D., and Coauthors, 2011: The Era-Interim reanalysis: Configuration and performance of the data assimilation system. Quarterly Journal of the royal meteorological society, 137 (656), 553–597.

Heil, A., Kaiser, J. W., van der Werf, G. R., Wooster, M. J., Schultz, M. G., and Dernier van der Gon, H. , 2010: Assessment of the Real- Time Fire Emissions (GFASv0) by MACC, Tech. Memo, 628, ECMWF, Reading, UK.

Iacono, M. J., J. S. Delamere, E. J. Mlawer, M. W. Shephard, S. A. Clough, and W. D. Collins, 2008: Radiaitve forcing by long-lived greenhouse gases: Calculations with the AER radiative transfer models, J. Geophys. Res., 113, D13103, doi:10.1029/2008JD0099443.

Kaiser, J., and Coauthors, 2012: Biomass burning emissions estimated with a global fire assimilation system based on observed fire radiative power. Biogeosciences, 9 (1), 527.

Kaiser, J. W., A. Heil, M. O. Andreae, A. Benedetti, N. Chubarova, L. Jones, J.-J. Morcrette, M. Razinger, M. G. Schultz, M. Suttie, and G. R. van der Werf: Biomass burning emissions estimated with a global fire assimilation system based on observed fire radiative power, Biogeosciences, 9, 527-554, 2012, doi:10.5194/bg-9-527-2012.

Lamarque, J.-F., T. C. Bond, V. Eyrin, C. Granier, A. Heil, Z. Klimont, D. Lee, C. Liousse, A. Mieville, B. Owen, M. G. Schultz, D. Shindell, S. J. Smith, E. Stehfest, J. Van Aardenne, O. R. Cooper, M. Kainuma, N.Mahowald, J. R. McConnell, V. Naik, K. Riahi, and D. P. van Vuuren, 2010: Historical (1850-2000) gridded anthropogenic and biomass burning emissions of reactive gases and aerosols: methodology and application, Atmos. Chem. Phys., 10, 7017-7039, doi:10.5194/acp-10-7017-2010.

Lamarque, J.-F., and Coauthors, 2010: Historical (1850–2000) gridded anthropogenic and biomass burning emissions of reactive gases and aerosols: methodology and application. Atmospheric Chemistry and Physics, 10 (15), 7017–7039.

Lau, W. K., and K.-M. Kim, 2010: Fingerprinting the impacts of aerosols on long-term trends of the Indian summer monsoon regional rainfall. Geophysical Research Letters, 37 (16).

Leutbecher, M., and Coauthors, 2017: Stochastic representations of model uncertainties at ECMWF: State of the art and future vision. Quarterly Journal of the Royal Meteorological Society, doi:10.1002/qj.3094, URL http://dx.doi.org/10.1002/qj.3094, qJ-16-0325.R1.

Lin, S. J. and R. B. Rood, 1996: Multidimensional flux-form semi-Lagrangian transport schemes, Mon. Weather Rev., 124, 2046-2070.

Lohmann, U. and E. Roeckner, 1996: Design and performance of a new cloud microphysis scheme developed for the ECHAM general circulation model, Climate Dyn., 12, 557-572.

Lohmann, U., Stier, P., Hoose, C., Ferrachat, S., Kloster, S., Roeck- ner, E., and Zhang, J., 2007: Cloud microphysics and aerosol indirect effects in the global climate model ECHAM5-HAM, Atmos. Chem. Phys., 7, 3425–3446, doi:10.5194/acp-7-3425-2007.

Morcrette, J.-J., and Coauthors, 2009: Aerosol analysis and forecast in the European Centre for Medium-Range Weather Forecasts Integrated Forecast System: Forward modeling. J. Geophys. Res., 114, doi:10.1029/2008JD011235.

Ramanathan, V., and Coauthors, 2005: Atmospheric brown clouds: Impacts on South Asian climate and hydrological cycle. Proceedings of the National Academy of Sciences of the United States of America, 102 (15), 5326–5333.

Reddy, M. S., O. Boucher, N. Bellouin, M. Schulz, Y. Balkanski, J.-L. Dufresne, and M. Pham, 2005: Estimates of global multicomponent aerosol optical depth and direct radiative perturbation in the laboratoire de meteorologie dynamique general circulation model. J. Geophys. Res.,110, doi:10.1029/2004JD004757.

Roeckner, E., G.Baeuml, L. Bonventura, R. Brokopf, M. Esch, M. Giorgetta, S. Hagemann, I. Kirchner, L. Kornblueh, E. Manzini, U. Rhodin, U. Schlese, U. Schulzweida, A. Tomkins, 2003: The atmospheric general circulation model ECHAM5. Part I: Model description, Report 349, Max Planck Institute for Meteorology, Hamburg, Germany.

Schrage, J. M. and Fink, A. H.: Nocturnal continental low-level stratus over tropical West Africa: observations and possible mechanisms controlling its onset, Mon. Wea. Rev., 140, 1794–1809, 2012.

Schuster, R., Fink, A. H., and Knippertz, P.: Formation and maintenance of nocturnal low-level stratus over the southern West African monsoon region during AMMA 2006, J. Atmos. Sci., 70, 2337–2355, 2013.

Stevens, B., M. Giorgetta, M. Esch, T. Mauritsen, T. Crueger, S. Rast, M. Salzmann, H. Schmidt, J. Bader, K. Block, R. Brokopf, I. Fast, S. Kinne, L. Kornblueh, U. Lohmann, R: Pincus, T. Reichler, and E. Roeckner, 2013: Atmospheric component of the MPI-M Earth System Model: ECHAM6, James, 5, 146-172, doi:10.1002/jame.20015.

Stier, P., J. Feichter, S. Kinne, S. Kloster, E. Vignati, J. Wilson, L. Ganzeveld, I. Tegen, M. Werner, Y. Balkanski, M. Schulz, O. Boucher, A. Minikin, and A. Petzold, 2005, The aerosol-climate model ECHAM5- HAM, Atmos. Chem. Phys., 5, 1125-1156.

Sundqvist, H., E. Berge, and J. E. Kristjansson, 1989, Condensation and Cloud Parameterization studies with a mesoscale numerical weather prediction model, Mon. Weather Rev., 117, 1641-1657.

Vignati, E., J. Wilson, and P. Stier, 2004, An efficient size-resolved aerosol microphysics module for large- scale aerosol transport models, J. Geophys. Res., 109, D22202, doi:10.1029/2003JD004485.

Vitart, F., 2014: Evolution of ecmwf sub-seasonal forecast skill scores. Quarterly Journal of the Roy. Meteor. Soc., 140, 1889–1899.

Zhang, K., D. O'Donnell, J. Kazil, P. Stier, S. Kinne, U. Lohmann, S. Ferrachat, B. Croft, J. Quaas, H. Wan, S. Rast, and J. Feichter, 2012: The global aerosol-climate model ECHAM-HAM, version 2: sensitivity to improvements in process representations, Atmos. Chem. Phys., 12, 8911-8949, doi:10.5194/acp-12-8911- 2012.